DISPERSION AND ASYMMETRY OF CHIRAL GRAVITATIONAL WAVES IN GYROSCOPIC MECHANICAL SYSTEMS. PART 1: DISCRETE LATTICE STRIPS

by A. KANDIAH, I. S. JONES, N. V. MOVCHAN and A. B. MOVCHAN[†]

(Department of Mathematical Sciences, University of Liverpool, Liverpool L69 7ZL, UK)

[Received October 17, 2024. Revised March 27, 2025. Accepted April 6, 2025]

Summary

The present paper introduces the notion of chiral gravitational elastic waves and explores their connections to equatorial and planetary waves. The analysis of the gravity-induced waveforms in gyroscopic systems composed of gyropendulums provides important insights into the dynamics of waves in the vicinity of the equatorial belt. We show that the direction of motion of the chiral waveforms can be controlled by choosing the orientation of the spinners. The presence of gravity is shown to affect the stop band frequencies for such structures, providing an additional control parameter for the chiral waveguides. The theoretical work is accompanied by illustrative examples.

1. Introduction

A chain of gyroscopic spinners, connected by elastic springs, and subjected to gravity, forms a physically chiral system. The dispersion properties of waves in one-dimensional physically chiral waveguides have been studied in (**1**), with the gyricity of gyroscopic spinners and gravity providing important control parameters of the dispersion of elastic waves in such waveguides, where the gyroscopic action couples the transverse components of the velocity field. In the present study, our motivation is linked to the analysis of the vibration of a discretised system along the equatorial region of a rotating sphere, where the important features include gravity and the gyroscopic force of inertia (also known as the Coriolis force). These effects significantly change the dispersion properties of the elastic waves, which take into account the physical chirality of the structure and the low-frequency band gaps due to the presence of gravity.

The recent interest in the analysis of continuous and discrete metamaterials, representing multiple beam structures with internal resonances, is apparent due to their wide range of important physical applications. The papers (**2**, **3**) develop new dynamic continualisation schemes and analyse block lattice metamaterials which include periodic arrangements of regular rigid blocks connected by linear elastic interfaces, that may also possess chiral properties. In this instance, the chirality results from a rotation of the blocks due to the special type of elastic connections, resulting in new dispersive behaviour of waves. The earlier study considering geometrically chiral metamaterial structures was

[†]Corresponding author <abm@liverpool.ac.uk>

Q. Jl Mech. Appl. Math, Vol. 78. No. 2 © The Author, 2025. Published by Oxford University Press.

https://doi.org/10.1093/qjmam/hbaf004

published in (**4**), where the geometric configuration of the system was shown to provide a coupling between shear and pressure waves. The investigation of the nonlocal continualisation schemes for lattice beams and plates can be found in (**5**), where various structural models are proposed to capture the scale effects in lattice-based structures, focusing on the stability and vibration analysis as well as the boundary conditions. The paper (**6**) addresses the dispersion of elastic waves in a locally resonant metamaterial structure, with spring-mass subsystems, which is an effective approach in modern designs of metamaterials.

The papers (**7, 8**) explore the localised stress distribution in dry masonry walls using experimental and theoretical approaches. In the framework of modern terminology, these papers are about block lattice metamaterials and their continuum approximation. The paper (**7**) examines experimentally how localised stress paths and stress concentrations occur due to the special pattern, associated with brick walls, and the connections between individual bricks. The analysis in (**8**) focuses on the continuous modelling representing a masonry wall as a highly anisotropic material. The work shows the importance on how the block structure of the metamaterial and the effective material properties affect the stress distribution. The paper (**9**) presents a further study investigating the modelling of crosswise tension resistance between compressed masonry layers, which results in significant tension perpendicular to the direction of compression. This demonstrates the range of important applications for mechanical block lattice metamaterials.

A review of the recent developments in the field of metamaterials can be found in (**10**), which includes the discussion of the theoretical, computational and experimental studies of elastic and acoustic metamaterials with their engineering applications. The study of wave propagation in mechanical metamaterials has led to advancements in mathematical modelling and characterisation techniques as detailed in (**11**). Recent studies on block lattice metamaterials (**12**) and topological metamaterials (**13**) have shown how specific lattice designs can exhibit unique phononic band gaps and mechanical properties. Examples of metamaterials characterised by geometrical chirality, such as twisted kagome lattices, are discussed in the paper (**14**), which highlights the significance of symmetry in shaping the phononic landscape, and the implications of geometric and functional duality in structural lattices of beams.

Dispersion of waves in infinite doubly periodic gyroscopic elastic systems has been analysed in (**15**), in systems of uniform gyricity, with no gravity. In this case, the dispersion relations are symmetric relative to the reversal of the direction of the wave vector. The gyroscopic spinners act as frequency splitters, as discussed in (**15–17**). A new effect of gyroscopic asymmetry, characterised by the one-way asymmetric waveforms on the interface between two physically chiral distinct structured half-planes was studied in (**18, 19**). In the present paper, we study a new physically chiral system, representing a one-dimensional structured waveguide of variable gyricity, which is also subjected to gravity. We analyse the case when the dispersion diagram becomes asymmetric. Two types of boundary conditions are also shown to influence the dispersion of chiral elastic waves in such a waveguide. The motivation for this study was a natural phenomenon of equatorial waves on a rotating sphere, with the special emphasis on the equatorial band, also known as the double Hadley cell (see, for example, (**20, 21**)). In terms of relevant physical phenomena, additional discussions, related to Kelvin waves, inertia-gravity waves and Rossby waves, can be found in (**22–27**).

A discrete model of a chiral elastic lattice strip with connecting gyroscopic pendulums is introduced in this paper, where gravity is present in the system. We show that gravity-induced waves also occur in the discrete strip with propagating waveforms associated with equatorial waves. In atmospheric dynamics, the Coriolis effect due to the planet's rotation is pivotal in the analysis of wave motions (**28, 29**). A novel analysis of equatorial waves is presented in the second part of this

study, in connection with the shallow water equations, which is applicable to studying waveforms on a thin strip.

The analysis of waveguides in multi-scale structured systems leads to the emergence of chiral vortex waves (see, for example, (**1**, **15**, **18**, **19**, **30**–**35**)), which includes the presence of gyroscopic components in discrete chiral structures. In fluid dynamics, atmospheric waves may exhibit distinctive rotational properties, leading to the formations of vortices and circulatory wave patterns. We show that the fundamental characteristics of chiral vortex waves, in the context of atmospheric dynamics, can be simply described by the introduction of gyroscopic spinners in a discrete lattice structure, without the need for a full Computational Fluid Dynamics (CFD) analysis. In this case, the presence of spinners results in a gyroscopic coupling of the velocity components and can be used to approximate the rotational behaviour of atmospheric wave phenomena.

Our investigation offers a new mathematical framework for modelling the nature of wave propagations within equatorial bands. We demonstrate that the large-scale atmospheric chiral wave motions in the equatorial zone can be approximately analysed in the context of a discrete lattice strip consisting of gyropendulums. A rigorous study of an elementary gyropendulum together with its motion can be found in (**1**). The Floquet–Bloch method is used to analyse wave propagation phenomena near the equatorial region through a discrete lattice model. We also present a three-dimensional chiral lattice structure that resembles the equatorial region. The vibrational modes of the three-dimensional model show that, when the orientation of the spinners is chosen in connection with the Coriolis effect, the structure exhibits eastward and westward oscillations, which are similar to equatorial waveforms. A detailed study of gravity's impact on the wave dynamics, particularly through the eigenfrequency analysis of two-dimensional lattice strips, is presented in this paper.

The paper is structured as follows. In Section 2, we introduce a three-dimensional chiral discrete and finite structure, subjected to the effects of gravity, and its eigenfrequencies and corresponding eigenmodes are investigated. The structure is constructed using an independent finite element model in COMSOL Multiphysics. Next, we develop a new mathematical lattice model of a gyro-elastic strip containing gyroscopic pendulums, together with illustrative examples, in Section 3. We investigate how the combined presence of gyroscopic spinners and gravity determine the vibrations of the strip for two different boundary conditions applied to the outer boundaries. The dispersion diagrams are examined for various configurations of the strip, and the important application to atmospheric wave phenomena in equatorial regions is discussed. In Section 4, we give some concluding remarks from the present work. Illustrative videos of the examples presented in this paper can be found in the electronic Supplementary Material.

2. Physical motivation and illustrative simulation of vibrations in a chiral belt

In this section, we discuss vibration modes of a finite three-dimensional belt composed of nodal points, connected by elastic trusses, and subjected to gyroscopic and gravitational forces; the simulation being produced in COMSOL Multiphysics 6.1. The main feature of this structure is the variable action of the gyroscopic forces within the belt. The structure consists of three horizontal circular rings of nodal points. There are no gyroscopic actions on the nodal points in the central ring, while the gyroscopic effects acting on the nodal points in the upper and lower rings are the same in magnitude and opposite in sign. In nature, there is an example of a similar gyroscopic system: it is the band incorporating the pair of Hadley cells in the equatorial region of the planet Earth.

Figure 1(a) shows a surface plot of the numerical data for equatorial oceanic waves on 3 January 2023. The equatorial waves are clearly visible, and they are confined within a band, known as the

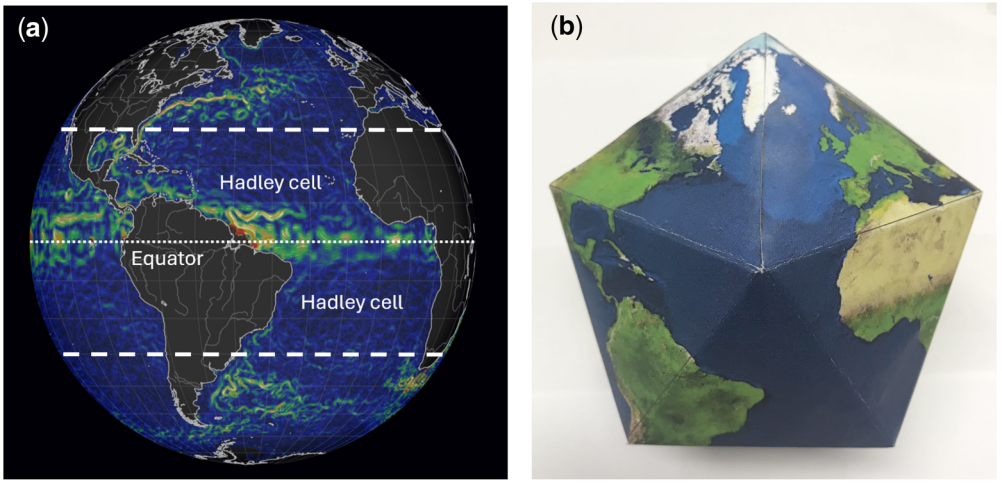

Fig. 1 (a) Waves in the equatorial region of the Earth, on 3 January 2023, reproduced from https://earth.nullschool.net/#2023/01/03/1700Z/ocean/surface/currents/orthographic=-45.00,0.00,332. The positions of the equator, as well as the upper and lower Hadley cells, are also shown. (b) Earth icosahedron

double Hadley cell. This band, which includes the tropical zone of Earth, is influenced by gravity and the Coriolis effect: the Coriolis force changes its sign as we cross the equator. In the upper Hadley cell, the Coriolis force deflects a moving object to the right, while in the lower Hadley cell, the Coriolis force deflects a moving object to the left. In part 2 of the paper, we discuss Kelvin, inertia-gravity and Rossby waves, which are important phenomena in atmospheric and oceanic dynamics in the equatorial region.

A simple lattice visualisation is given by the Earth icosahedron (see Fig. 1(b), this three-dimensional model has been assembled using the map from https://solarviews.com/cap/ico/icoearth.htm), which is commonly used in meteorology and Earth Science. Based on this visualisation, one can triangulate the sphere into 20 equilateral spherical triangles, whose vertices coincide with the vertices of the Earth icosahedron. Although it is not possible to continue the refinement of the triangulation of the entire sphere to obtain an analogue of the doubly periodic triangular lattice on a plane, it is feasible to continue the triangulation of the equatorial belt by reducing the size of the elementary cell, as is done in an infinite strip in a plane. Furthermore, Floquet–Bloch theory can be used to study approximations of gravity-induced equatorial waves, subjected to the Coriolis force.

In Fig. 2, we show illustrative computations for a lattice chiral belt consisting of massless elastic links connecting the inertial junctions. The Coriolis effect is modelled by gyroscopic forces, so that in the lattice structure they are orthogonal to the nodal point velocities at each junction. The gyroscopic force acting on the i-th nodal point is defined by $\mathbf{F}_i = m_i(\boldsymbol{\Omega}_i \times \mathbf{v}_i)$, where m_i is the mass, $\mathbf{v}_i$ is the velocity vector and $\boldsymbol{\Omega}_i = \Omega(\cos(\theta_i), \sin(\theta_i), 0)$ is the gyricity vector with Ω representing the gyricity parameter. The angle θ_i denotes the azimuth angle in the xy-plane of the i-th nodal point relative to the centre of the corresponding ring from the x-axis, with $0 \leq \theta_i < 2\pi$. In particular, since there are no gyroscopic forces acting on the nodal points in the central ring, then $\Omega = 0$ rad/s for such points. The gyricity parameters for the nodal points in the lower and upper rings are Ω and $-\Omega$, respectively, as discussed above. Moreover, gravity is modelled as an additional force on each

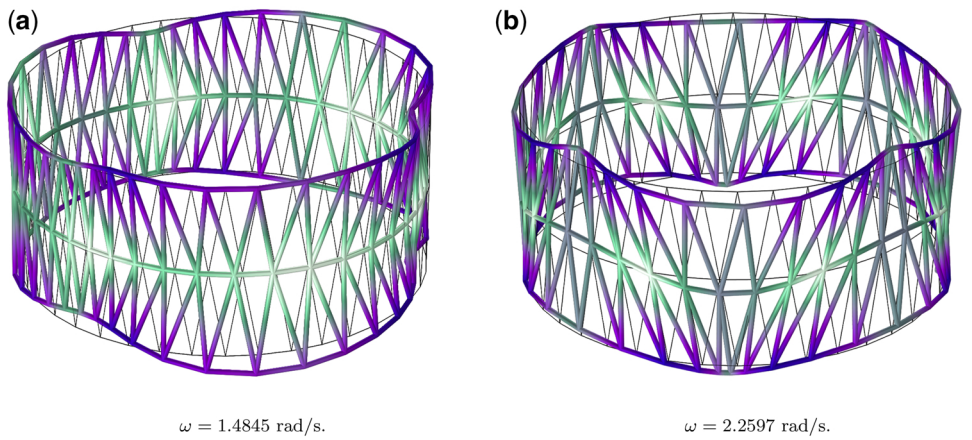

Fig. 2 Eigenmodes of the chiral belt with (a) horizontal and (b) vertical oscillations of the nodal points in the central ring. Gyroscopic forces are present for the nodal points in the upper and lower rings, while there are no gyroscopic actions on the nodal points in the central ring. Gravitational forces are present at each nodal point and act uniformly. The magnitudes of the gyroscopic and gravitational parameters are both chosen to be unitary. The eigen frequencies of the modes are: (a) $\omega = 1.4845$ rad/s and (b) $\omega = 2.2597$ rad/s

nodal point acting radially inwards towards the centre of each horizontal ring. In the FE model, each nodal point is connected to its nearest neighbouring nodal point by massless and elastic links. We compute the eigenfrequencies and eigenmodes of the three-dimensional structure and show the existence of linearly tangential oscillations along the central ring, with either eastward or westward propagations of the individual wave components. These modes are linked to the standing modes of an infinite discrete two-dimensional chiral lattice strip. This characteristic resembles the zonally propagating equatorial waves detailed in part 2, which includes the analysis of waves in narrow equatorial bands described by the shallow water equations. In Fig. 2, we present examples of the chiral belt eigenmodes for the case where each nodal point has a mass of 1kg, connected by links of length 1m, and the gyricity parameter is chosen as $\Omega = 1$ rad/s. In the illustrative examples, each ring of the chiral belt consists of 40 nodal points, and the gravitational force acts uniformly and radially inwards for each ring with the unit magnitude. The eigenmodes of the belt are shown for two different eigenfrequencies. The horizontal vibrations of the nodal points positioned along the central ring, inducing eastward-propagating waveforms are shown in Fig. 2(a) with $\omega = 1.4845$ rad/s. Conversely, the mode presented in Fig. 2(b) corresponds to vertical tangential motions with localised horizontal vibrations of the nodal points in the central ring for $\omega = 2.2597$ rad/s. The latter frequency also displays eastward-moving oscillations along the structure. Additionally, the nodal point trajectories in Fig. 2(a) for the upper and lower rings move in a counterclockwise and clockwise direction, respectively, while for the same nodal points, the trajectories are traced in a clockwise and counterclockwise direction in Fig. 2(b). This occurs due to the change in eigenfrequency, the gyroscopic forces imposed on the masses in the upper and lower rings, together with the linear harmonic motion of the nodal points in the central ring. Illustrative videos of the eigenmodes can be found in the electronic Supplementary Material provided with this paper.

In the context of equatorial waves, inertia-gravity waves can exhibit horizontal (zonal) and vertical (meridional) motions, which is a similar feature of the nodal points presented in the eigenmodes

of the FE model. The three-dimensional chiral belt offers a simple yet effective approximate representation of equatorial waves. In particular, the model takes into account the Coriolis effect within the equatorial region of the Earth, through the gyroscopic forces for each nodal point. In addition to the above illustration of the dynamics of a three-dimensional lattice belt subjected to gyroscopic forces, we also note the continuous approximations of the equatorial waves, discussed in (**24, 25**), where the idea of transverse exponential localisation has been used. The detailed consideration of such an approximation, in comparison with the formulation associated with a finite-width strip, is included in part 2 of the paper.

3. Elastic chiral lattice strip subjected to gravity

In this section, we present a structured study of dispersive waves in an infinite chiral elastic strip subjected to gravity, with two different types of boundary conditions (Neumann or Dirichlet conditions) prescribed on the outer layers of the strip. The effects of gravity and chirality are introduced through the gyroscopic pendulums embedded at the junctions of the strip (see (**1**)). The dispersion properties for the elastic lattice strip are studied, and it is shown that one can control the preferential direction of the uni-directional waveforms and the locations of stop bands by tuning the gyricity and gravity parameters. The analysis of the waveforms corresponding to frequencies near the touching and crossing points of the dispersion curves is provided in Appendix A, illustrating diverse standing wave patterns and interference phenomena. The gyroscopic lattice strip models presented here have no external energy flux and are referred to as passive gyroscopic systems. A detailed examination on the dynamics of an active Dirichlet lattice strip is provided in Appendix B.

3.1. *Chiral gravitational lattice strip with Dirichlet boundary conditions*

We consider an infinite chiral lattice strip of horizontal layers with Dirichlet boundary conditions, containing embedded gyroscopic pendulums. The Dirichlet boundary conditions are set on the outer horizontal boundaries of the five-layered strip shown in Fig. 3. Conversely, the Neumann problem for the three-layer strip is investigated in Section 3.3. The pendulum feature of the structure allows for a description of the problem in the presence of gravitational forces, while the gyroscopic effect is taken into account by the properties of the spinners. For both the Dirichlet and Neumann problems, the strip system consists of three infinite horizontal rows of gyropendulums suspended from their pivot points so that they can swing freely under gravity, and each nodal point is connected to its nearest neighbours by elastic links. We formulate the governing equations for the nodal points and analyse the types of propagating waves in such systems. The periodicity of the model allows for the application of Floquet–Bloch theory.

In the undisturbed configuration, the axis of each gyropendulum arm is perpendicular to the xy-plane. When the lattice nodes move, the spinners exert a force perpendicular to the displacement of the nodal point. In our analysis, the gyropendulums are assumed to undergo small-amplitude oscillations with minimal deviations from their equilibrium state, confining the lattice particles to move in the xy-plane.

3.1.1. Governing equations. We formulate the governing equations of the problem and describe the waves that can propagate in a discrete elastic Dirichlet strip. The nodes at the junctions of the structure are assumed to be the same and each nodal point is connected to its nearest neighbour by massless springs of length l and stiffness c. The displacements at each point are assumed to be small so that the motion of the structure can be described by linear equations.

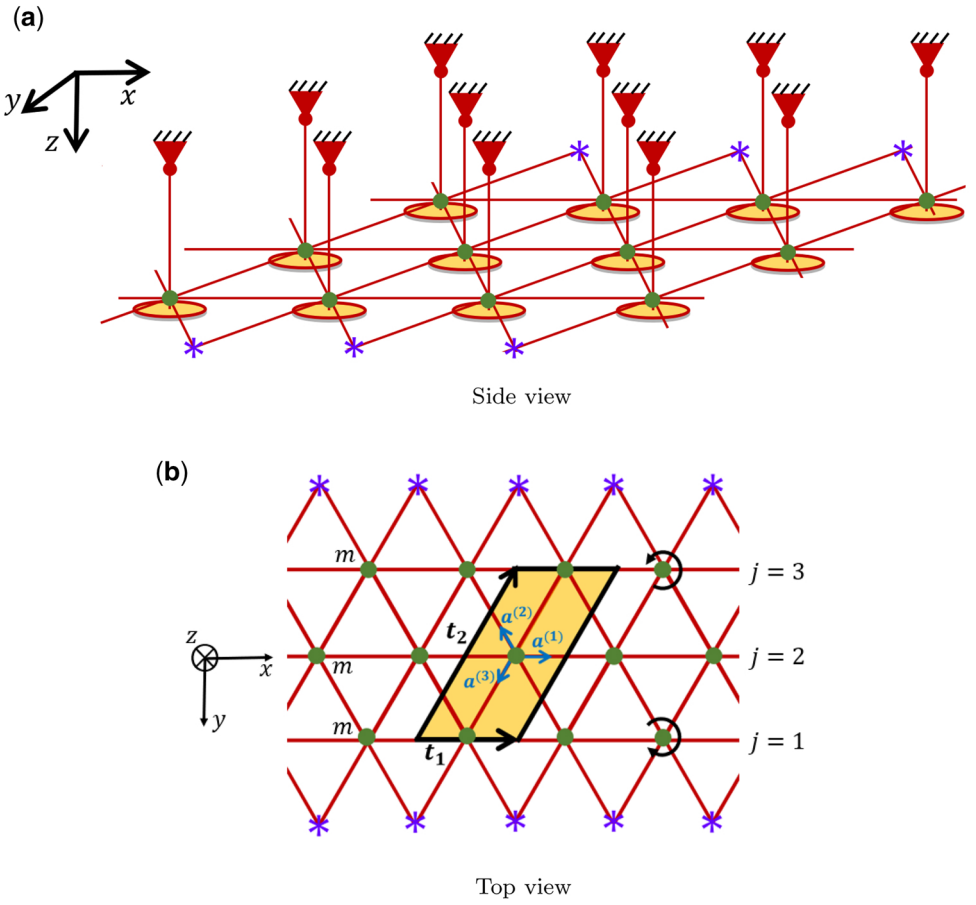

Fig. 3 Chiral gravitational lattice strip consisting of nodal points connected by elastic springs, which are attached to gyropendulums (with gravity acting in the positive z-direction). Dirichlet boundary conditions are prescribed in the y-direction and the lattice strip is infinite in the x-direction; (a) side view and (b) top view

The lattice strip, with the elementary cell shown in Fig. 3(b), includes three nodal points and the lattice vectors characterising the elementary parallelogram cell are

$$\mathbf{t}_1 = l(1,0)^T, \quad \mathbf{t}_2 = l(1,\sqrt{3})^T. \tag{3.1}$$

We note that the lattice system is periodic along the x-axis, and its periodicity is defined by the lattice vector $\mathbf{t}_1$.

It is assumed that the nodal points in the inner layers of the strip, that is for $j = 1, j = 2$ and $j = 3$, have masses m. We also introduce the three unit vectors $\mathbf{a}^{(j)}$, $j = 1,2,3$, representing the directions

of links within the elementary cell:

$$\mathbf{a}^{(1)} = (1,0)^T, \quad \mathbf{a}^{(2)} = \left(-\frac{1}{2}, \frac{\sqrt{3}}{2}\right)^T, \quad \mathbf{a}^{(3)} = \left(-\frac{1}{2}, -\frac{\sqrt{3}}{2}\right)^T. \tag{3.2}$$

The position vector of the mass on the j-th layer ($j = 1,2,3$) is given by

$$\mathbf{x}^{(n,j)} = \mathbf{x}^{(0,j)} + n\mathbf{t}_1, \tag{3.3}$$

where n is the integer index, $\mathbf{x}^{(0,j)}$ is the position of a reference particle in the Dirichlet strip and the vector $\mathbf{t}_1$ is defined in (3.1).

The lattice strip shown in Fig. 3 consists of gyroscopic spinners attached at every junction except those in the outer layers (shown by purple asterisks), which correspond to fixed points in accordance with the Dirichlet boundary conditions. Each gyropendulum consists of a massless rod, that is perpendicular to the plane of the two-dimensional lattice strip. The gyroscopic spinners generate a moment creating a 'vortex-type' motion of the structure.

The elementary cell of the periodic structure, shown in Fig. 3(b), includes three particles, whose in-plane displacements are denoted by $\mathbf{u}^{(n,j)}$, for $j = 1,2,3$. The displacements are assumed to be time-harmonic with the radian frequency ω. Then the equations of motion for the three lattice masses in the time-harmonic regime are as follows:

$$\begin{aligned} -\tfrac{m\omega^2}{c}\mathbf{u}^{(n,1)} = {} & (\mathbf{a}^{(1)} \cdot (\mathbf{u}^{(n+1,1)} - \mathbf{u}^{(n,1)}))\mathbf{a}^{(1)} + (\mathbf{a}^{(1)} \cdot (\mathbf{u}^{(n-1,1)} - \mathbf{u}^{(n,1)}))\mathbf{a}^{(1)} \\ & + (\mathbf{a}^{(2)} \cdot (\mathbf{u}^{(n-1,2)} - \mathbf{u}^{(n,1)}))\mathbf{a}^{(2)} + (\mathbf{a}^{(3)} \cdot (\mathbf{u}^{(n,2)} - \mathbf{u}^{(n,1)}))\mathbf{a}^{(3)} \\ & + i\tfrac{m\Omega\omega}{c}\mathbf{R}\mathbf{u}^{(n,1)} - \tfrac{mG}{c}\mathbf{u}^{(n,1)} - (\mathbf{a}^{(2)} \cdot \mathbf{u}^{(n,1)})\mathbf{a}^{(2)} - (\mathbf{a}^{(3)} \cdot \mathbf{u}^{(n,1)})\mathbf{a}^{(3)}, \end{aligned} \tag{3.4}$$

$$\begin{aligned} -\tfrac{m\omega^2}{c}\mathbf{u}^{(n,2)} = {} & (\mathbf{a}^{(1)} \cdot (\mathbf{u}^{(n+1,2)} - \mathbf{u}^{(n,2)}))\mathbf{a}^{(1)} + (\mathbf{a}^{(1)} \cdot (\mathbf{u}^{(n-1,2)} - \mathbf{u}^{(n,2)}))\mathbf{a}^{(1)} \\ & + (\mathbf{a}^{(2)} \cdot (\mathbf{u}^{(n-1,3)} - \mathbf{u}^{(n,2)}))\mathbf{a}^{(2)} + (\mathbf{a}^{(2)} \cdot (\mathbf{u}^{(n+1,1)} - \mathbf{u}^{(n,2)}))\mathbf{a}^{(2)} \\ & + (\mathbf{a}^{(3)} \cdot (\mathbf{u}^{(n,1)} - \mathbf{u}^{(n,2)}))\mathbf{a}^{(3)} + (\mathbf{a}^{(3)} \cdot (\mathbf{u}^{(n,3)} - \mathbf{u}^{(n,2)}))\mathbf{a}^{(3)} - \tfrac{mG}{c}\mathbf{u}^{(n,2)}, \end{aligned} \tag{3.5}$$

and

$$\begin{aligned} -\tfrac{m\omega^2}{c}\mathbf{u}^{(n,3)} = {} & (\mathbf{a}^{(1)} \cdot (\mathbf{u}^{(n+1,3)} - \mathbf{u}^{(n,3)}))\mathbf{a}^{(1)} + (\mathbf{a}^{(1)} \cdot (\mathbf{u}^{(n-1,3)} - \mathbf{u}^{(n,3)}))\mathbf{a}^{(1)} \\ & + (\mathbf{a}^{(2)} \cdot (\mathbf{u}^{(n+1,2)} - \mathbf{u}^{(n,3)}))\mathbf{a}^{(2)} + (\mathbf{a}^{(3)} \cdot (\mathbf{u}^{(n,2)} - \mathbf{u}^{(n,3)}))\mathbf{a}^{(3)} \\ & - i\tfrac{m\Omega\omega}{c}\mathbf{R}\mathbf{u}^{(n,3)} - \tfrac{mG}{c}\mathbf{u}^{(n,3)} - (\mathbf{a}^{(2)} \cdot \mathbf{u}^{(n,3)})\mathbf{a}^{(2)} - (\mathbf{a}^{(3)} \cdot \mathbf{u}^{(n,3)})\mathbf{a}^{(3)}, \end{aligned} \tag{3.6}$$

where $\boldsymbol{\Omega}$ is the gyricity parameter which depends on the geometry of the spinners, $G = g/L$ is the gravity parameter with L denoting the length of the pendulum arm, and $\mathbf{R}$ is the rotation matrix given by

$$\mathbf{R} = \begin{pmatrix} 0 & 1 \\ -1 & 0 \end{pmatrix}. \tag{3.7}$$

In our analysis, the gyricities of the nodal points along the central chain ($j = 2$) of the strip are chosen to be zero, while the gyricities in the lower ($j = 1$) and upper ($j = 3$) layers of nodal points are chosen to be the same in magnitude, but opposite in orientation. In the following analysis, we investigate the combined effects of the gyricity and gravity parameters on the waveforms in the discrete structure as well as the dispersion characteristics.

3.1.2. Elastic chiral gravitational Floquet–Bloch waves. The amplitudes of the time-harmonic displacements of the nodal points within the periodic vortex-type gravitational Dirichlet strip satisfy the system of Equations (3.4)–(3.6), together with the quasi-periodicity of the system characterised by the Floquet–Bloch conditions:

$$\mathbf{W}(\mathbf{r}+n\mathbf{t}_1)=\mathbf{W}(\mathbf{r})e^{iknl}, \tag{3.8}$$

where $\mathbf{W}=(u_x^{(1)},u_y^{(1)},u_x^{(2)},u_y^{(2)},u_x^{(3)},u_y^{(3)})$ is the displacement vector in the xy-plane, $\mathbf{r}=(x,y)^T$ is the position vector and k is the wavenumber.

By applying (3.8) into the system (3.4)–(3.6), we obtain the following system of equations in the matrix form:

$$[\mathbf{C}_D-\omega^2\mathbf{M}+\omega\mathbf{A}]\mathbf{W}=\mathbf{0}, \tag{3.9}$$

where $\mathbf{M}=m\mathbf{I}$ is the mass matrix ($\mathbf{I}$ is the 6×6 identity matrix),

$$\mathbf{A}=i\begin{pmatrix} 0 & -m\Omega & 0 & 0 & 0 & 0\\ m\Omega & 0 & 0 & 0 & 0 & 0\\ 0 & 0 & 0 & 0 & 0 & 0\\ 0 & 0 & 0 & 0 & 0 & 0\\ 0 & 0 & 0 & 0 & 0 & m\Omega\\ 0 & 0 & 0 & 0 & -m\Omega & 0 \end{pmatrix}, \tag{3.10}$$

is the spinner matrix, and

$$\mathbf{C}_D=-\begin{pmatrix} 2c[\cos(kl)-\frac{3}{2}]-mG & 0 & \frac{c}{4}(e^{-ikl}+1) & \frac{c\sqrt{3}}{4}(-e^{-ikl}+1) & 0 & 0\\ 0 & -3c-mG & \frac{c\sqrt{3}}{4}(-e^{-ikl}+1) & \frac{3c}{4}(e^{-ikl}+1) & 0 & 0\\ \frac{c}{4}(e^{ikl}+1) & \frac{c\sqrt{3}}{4}(-e^{ikl}+1) & 2c[\cos(kl)-\frac{3}{2}]-mG & 0 & \frac{c}{4}(e^{-ikl}+1) & \frac{c\sqrt{3}}{4}(-e^{-ikl}+1)\\ \frac{c\sqrt{3}}{4}(-e^{ikl}+1) & \frac{3c}{4}(e^{ikl}+1) & 0 & -3c-mG & \frac{c\sqrt{3}}{4}(-e^{-ikl}+1) & \frac{3c}{4}(e^{-ikl}+1)\\ 0 & 0 & \frac{c}{4}(e^{ikl}+1) & \frac{c\sqrt{3}}{4}(-e^{ikl}+1) & 2c[\cos(kl)-\frac{3}{2}]-mG & 0\\ 0 & 0 & \frac{c\sqrt{3}}{4}(-e^{ikl}+1) & \frac{3c}{4}(e^{ikl}+1) & 0 & -3c-mG \end{pmatrix}, \tag{3.11}$$

is the gravity-stiffness matrix. Equation (3.9) has non-trivial solutions if and only if the following condition is satisfied

$$\det[\mathbf{C}_D-\omega^2\mathbf{M}+\omega\mathbf{A}]=\sigma_D^{(1)}(m,G,\Omega,k,\omega,c,l)\sigma_D^{(2)}(m,G,\Omega,k,\omega,c,l)=0, \tag{3.12}$$

where

$$\sigma_D^{(1)}(m,G,\Omega,k,\omega,c,l) = m^3\omega^6 + (4c\cos(kl) - (\Omega^2+3G)m - 9c)m^2\omega^4$$
$$+(4c^2\cos^2(kl) - \left(\frac{47c}{2} + 2m(\Omega^2+4G)\right)c\cos(kl) + 26c^2 + 3(\Omega^2+6G)mc + Gm^2(\Omega^2+3G))m\omega^2$$
$$-\frac{\sqrt{3}\Omega c^2 m\omega\sin(kl)}{2} - 4G\cos^2(kl)c^2m - \frac{21\cos^2(kl)c^3}{2} + 4G^2\cos(kl)cm^2$$
$$+\frac{47G\cos(kl)c^2m}{2} + 33\cos(kl)c^3$$
$$-G^3m^3 - 9G^2cm^2 - 26Gc^2m - 24c^3, \tag{3.13}$$

and

$$\sigma_D^{(2)}(m,G,\Omega,k,\omega) = m^3\omega^6 + (2c\cos(kl) - (\Omega^2+3G)m - 9c)m^2\omega^4$$
$$+\left(G\Omega^2m^2 + 3G^2m^2 - 4G\cos(kl)cm + 3\Omega^2cm + 18Gcm - \frac{27\cos(kl)c^2}{2} + 24c^2\right)m\omega^2$$
$$+\frac{3\sqrt{3}\Omega c^2m\omega\sin(kl)}{2} - \frac{9\cos^2(kl)c^3}{2} + 2G^2\cos(kl)cm^2 + \frac{27G\cos(kl)c^2m}{2} + 18\cos(kl)c^3$$
$$-G^3m^3 - 9G^2cm^2 - 24Gc^2m - 18c^3. \tag{3.14}$$

Equation (3.12) is referred to as the dispersion relation of the Dirichlet lattice strip. The quantities (3.13) and (3.14) define the frequencies and wavenumbers of the waveforms associated with only horizontal and only vertical motions of the central nodal points, respectively, while the upper and lower nodal points follow elliptical trajectories as discussed in subsequent sections. The analytical forms of the trajectories are provided in Appendix C.

3.2. *Dispersion properties of the gyro-elastic chiral strip with Dirichlet boundary conditions*

We analyse the dispersion properties of a discrete Dirichlet strip subjected to gravity and demonstrate how the waveforms along the structure depend on the gravity and gyricity parameters. The analytical results are derived for the general parameter values. However, in the illustrative numerical examples, we focus on varying the gyricity and gravity, while the parameters l, c and m are chosen to be normalised as $l = 1, c = 1$ and $m = 1$. Also, the physical units of measurement will not be shown. In the following illustrative examples, we consider non-negative values of the gyricity parameter Ω.

Figure 4 shows the dispersion diagrams for different values of the gravity and gyricity parameters of the infinite lattice strip with Dirichlet boundary conditions. The dispersion diagrams can be used to select the different types of nodal trajectories of the Dirichlet lattice strip, in connection with propagating or standing waves. The solid dispersion curves correspond to zero vertical displacements of the central nodal points, while the dashed dispersion curves correspond to zero horizontal displacements of the central nodal points. The dispersion degeneracies linked to the crossing or touching points of the dispersion curves are discussed in Appendix A.

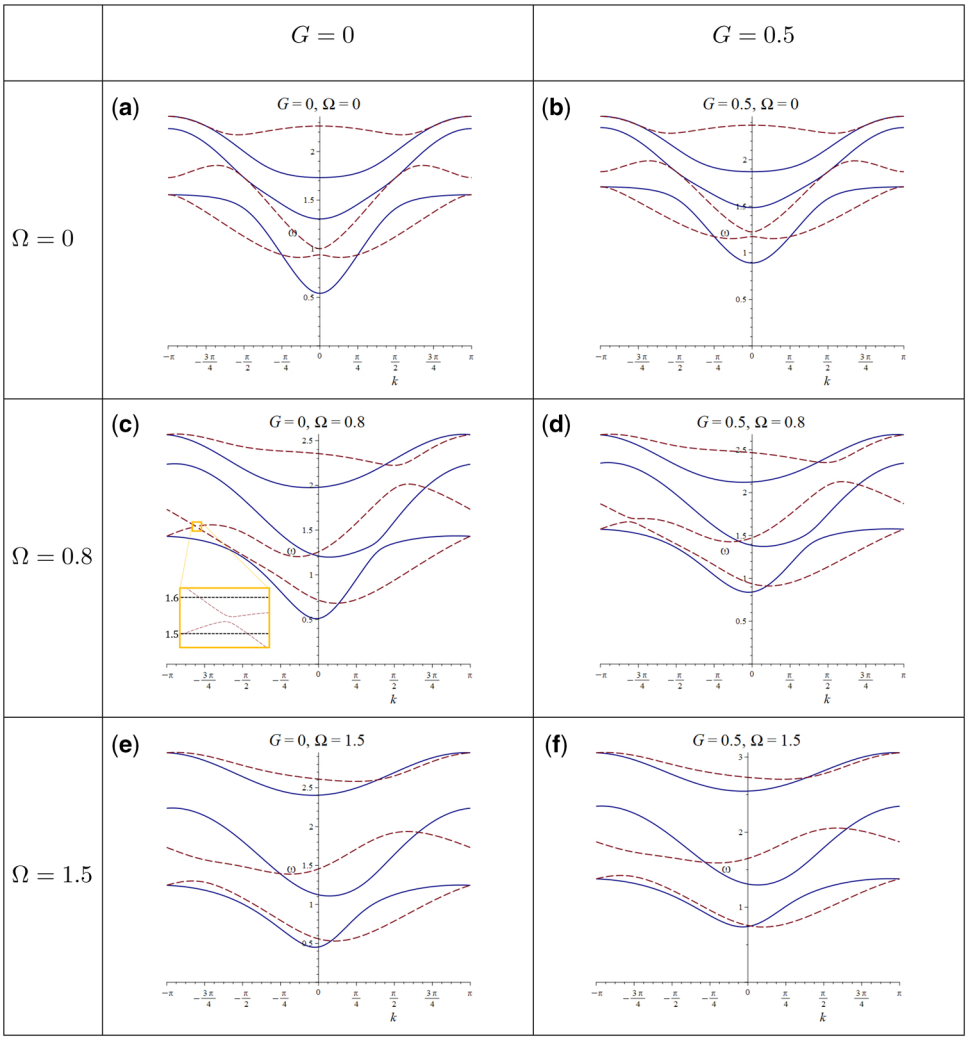

Fig. 4 Dispersion diagrams, illustrating the frequency ω against the wavenumber k, of the lattice strip for a range of values of the gravity and gyricity parameters. The normalised parameter values of the Dirichlet strip are $c = 1, l = 1$ and $m = 1$. The solid and dashed curves correspond to the solutions of (3.13) and (3.14), respectively, associated with the nodal point trajectories described in Section 3.1.2 and Appendix C

When both gravity and gyricity are absent in the Dirichlet lattice strip, the dispersion diagram is shown in Fig. 4(a); there is a zero frequency stop band as well as a cut-off frequency above which no propagating waveforms exist. It is noted that when $G = 0$ and $\Omega = 0$, there are standing modes present at $k = 0$, at the boundaries $k = \pm\pi$ as well as points within the first Brillouin zone, and the dispersion curves are symmetric with respect to the frequency axis. There are six curves in each dispersion diagram, and the right- and left-propagating waves are determined by taking into account

the locations of positive and negative slopes of the dispersion curves, respectively. In the presence of gravity and absence of gyricity, the dispersion diagram is shown in Fig. 4(b), where the size of the zero-frequency band gap increases, while the symmetry relative to the frequency axis of the dispersion curves remains as in the case with $G = 0$ and $\Omega = 0$. Introducing the gyricity through the spinners breaks the symmetry of the dispersion curves relative to $k = 0$ as demonstrated in Fig. 4, where the characteristics of physical chirality introduces a preferential directionality of the wave propagation. In addition when $\Omega \neq 0$, the points on the dispersion curves associated with standing waveforms, shift away from $k = 0$, resulting in asymmetry in the dispersion curves; these points correspond to zero group velocities and non-zero phase velocities, which are investigated below. For non-trivial gyricities, the lattice strip also exhibits propagating waves with positive (negative) group velocities and negative (positive) phase velocities, that can affect the complex interaction between the motion of the wave and its individual components. Increasing the gyricity Ω leads to a larger separation between the two high-frequency and two low-frequency dispersion curves, as well as additional finite-frequency intervals associated with stop bands, as shown in Fig. 4(e) and (f). In the limit $\Omega \to \infty$, the two lower curves approach zero, while the two intermediate dispersion curves approach the curves described by

$$\omega = \omega_1 = \sqrt{\frac{mG + 3c}{m}} = \text{const}, \ \omega = \omega_2(k) = \sqrt{\frac{mG + 3c - 2c\cos(kl)}{m}}. \tag{3.15}$$

We also note that the two upper curves increase for increasing Ω, with the frequencies being proportional to the gyricity parameter.

3.2.1. Propagating waveforms along the chiral Dirichlet strip. In this section, we present the typical trajectories of the nodal points in the Dirichlet strip introduced in Section 3.1. The motions of the nodal points are linked to the dispersion properties discussed in the previous section. The displacements of the fixed points shown in Fig. 3 are zero, while the nodal points within the inner layers, that is for $j = 1, 2, 3$, follow linear or elliptical trajectories (see also Appendix C).

In Fig. 5, we present the dispersion diagram of the Dirichlet lattice strip for the parameter values $G = 0.3$ and $\Omega = 0.3$. The points $\mathcal{A}, \mathcal{B}, \mathcal{C}, \ldots, \mathcal{H}$, correspond to examples of nodal point trajectories which are detailed below. Figure 5 also shows the definitions of the group and phase velocities of the waves, where the former represents the rate at which the overall shape of the wave packet propagates in connection with the transmitted energy, while the latter describes the rate at which the phase of an individual wave propagates in the strip. For a stationary wave, characterised by a pattern that does not propagate in the spatial direction, there is zero net transfer of energy and thus, the group velocity vanishes; the points $\mathcal{E}$ and $\mathcal{F}$ on the dispersion diagram are associated with standing waves. The points $\mathcal{A}, \mathcal{B}, \mathcal{C}$ and $\mathcal{D}$ on Fig. 5 correspond to four examples where the group velocity is non-zero, resulting in propagating waves along the infinite discrete chiral strip. The points of dispersion degeneracies, denoted by $\mathcal{G}$ and $\mathcal{H}$ correspond to two examples of crossing points of the dispersion curves (see Appendix A).

Illustrative trajectories of the nodal points at $k = 0$ are shown in Fig. 6, for two different frequency values. In Fig. 6(a), the central nodal points move in a vertical motion, with no horizontal displacement, while in the example shown in Fig. 6(b), the central nodal points are displaced only in the horizontal direction; these trajectories are associated with the points $\mathcal{A}$ and $\mathcal{B}$ in the dispersion diagram shown in Fig. 5. A characteristic feature of the Dirichlet strip geometry and the gyricity choices is the tendency of the nodal points in the upper ($j = 3$) and lower ($j = 1$) layers to move in

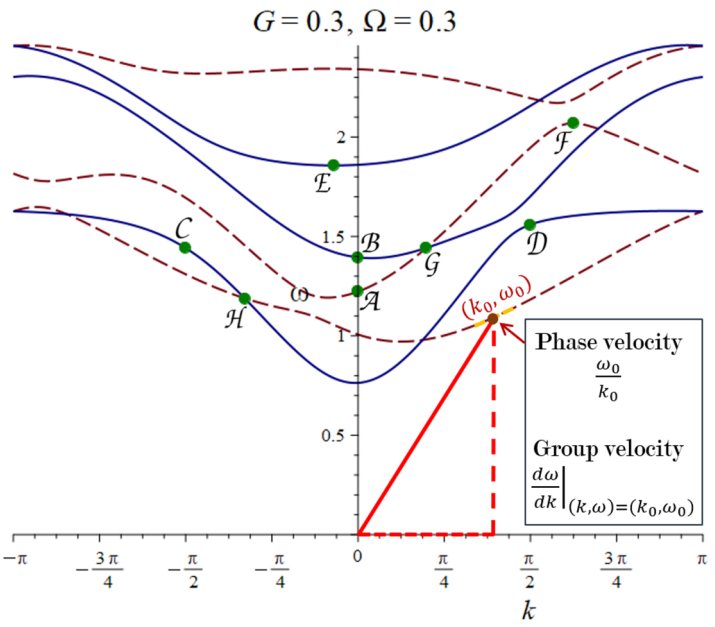

Fig. 5 Dispersion diagram for the chiral gravitational lattice ship shown in Fig. 3, for $G = 0.3$ and $\Omega = 0.3$. The remaining normalised physical quantities are $m = 1, c = 1$ and $l = 1$. The units of measurement will not be displayed. The definitions of the phase and group velocities at an arbitrary point (k_0, ω_0) are also defined. The solid dispersion curves are associated with zero vertical displacements of the central nodal points, while the dashed dispersion curves are linked to zero horizontal displacements of the central nodal points. The nodal point trajectories of the Dirichlet strip corresponding to the points $\mathcal{A}, \mathcal{B}, \mathcal{C}, \ldots, \mathcal{H}$, are discussed in the text

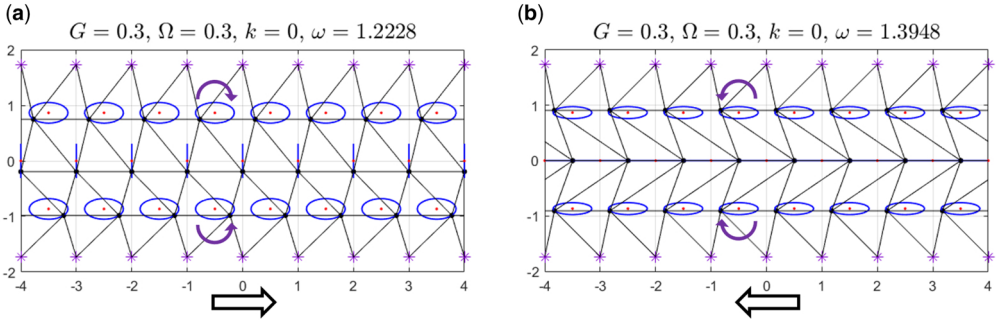

Fig. 6 Nodal point trajectories of the lattice strip for $k = 0$ and the parameter values $G = 0.3$ and $\Omega = 0.3$. The corresponding dispersion diagram is shown in Fig. 5 with the points $\mathcal{A}$ and $\mathcal{B}$ linked to parts (a) and (b), respectively; (a) $(k, \omega) = (0, 1.2228)$ and (b) $(k, \omega) = (0, 1.3948)$. The arrows denote the direction of the group velocity, and the circular arrows show the orientation of motion of the nodal points. The videos of the above trajectories can be found in the electronic Supplementary Material

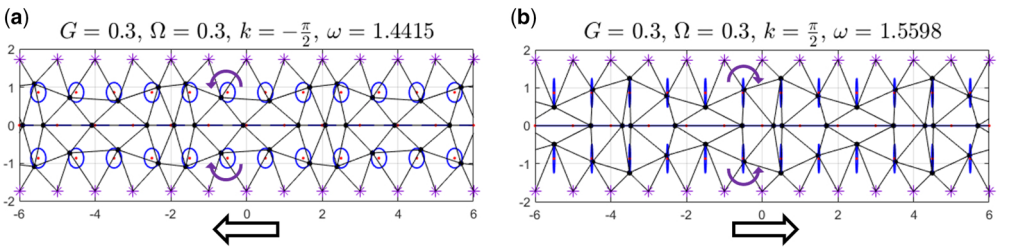

Fig. 7 Elliptical trajectories of the nodal points in connection with propagating waves. The associated dispersion diagram is shown in Fig. 5 with the points $\mathcal{C}$ and $\mathcal{D}$ corresponding to parts (a) and (b), respectively; (a) $(k,\omega) = (-\pi/2, 1.4415)$ and (b) $(k,\omega) = (\pi/2, 1.5598)$

opposite directions. In both the upper and lower layers of the strip, the nodal points follow ellipses with major axes aligned parallel to the direction of the wave motion. It is noted that although the propagating waveforms shown in Fig. 6 correspond to non-zero group velocities, the frequencies of the oscillations are near the standing mode frequencies of the structure, where the slope of the curves shown in Fig. 5 is zero. This occurs due to the non-trivial gyricity value resulting in asymmetric dispersion diagrams.

Additional examples of propagating wave solutions moving in the negative and positive x-directions in the Dirichlet strip are shown in Fig. 7(a) and (b), respectively. The frequencies in the illustrative examples displayed in Fig. 7 differ to those in Fig. 6. In the trajectories shown in Fig. 7, the central nodal points move only horizontally, while the upper and lower nodal points follow elliptical paths with major axes aligned perpendicular to the direction of the propagating waveforms. The dispersion diagram associated with the examples is shown in Fig. 5, where the frequency and wavenumber values in Fig. 7(a) and (b) correspond to $\mathcal{C}$ and $\mathcal{D}$, respectively. Analogous features are also observed for the inertia-gravity waves in the equatorial region as discussed in part 2.

Through the above illustrative examples, we observe that the frequencies alter the vibrational modes of the structure, impacting the trajectories of the nodal points, and thus, the oscillations and mode shapes of the Dirichlet lattice strip.

3.2.2. Standing modes of the discrete strip with Dirichlet boundary conditions. In this section, we display the standing modes behaviour of the Dirichlet strip through illustrative examples. The related dispersion diagram is presented in Fig. 5, where the wavenumber and frequency values corresponding to standing waves are marked by $\mathcal{E}$ and $\mathcal{F}$.

The standing mode patterns of the lattice strip for $\omega = 1.8572$ rad/s are shown in Fig. 8(a), with the central nodal points moving solely horizontally, whereas the upper and lower nodal points move in a clockwise and counterclockwise orientation, respectively. The standing wave with a higher frequency compared to the example presented in Fig. 8(a), is illustrated in Fig. 8(b) which corresponds to the vertically displaced central nodal points, while the upper and lower nodal point trajectories follow elliptical paths with major axes aligned perpendicular to the central horizontal layer. In both examples, the orientations and alignment of the nodal points in the lower ($j = 1$) and upper ($j = 3$) layers are similar, but the eccentricities of the ellipses differ as well as the motions of the central nodal points. The illustrative videos of the standing modes can be viewed in the electronic Supplementary Material.

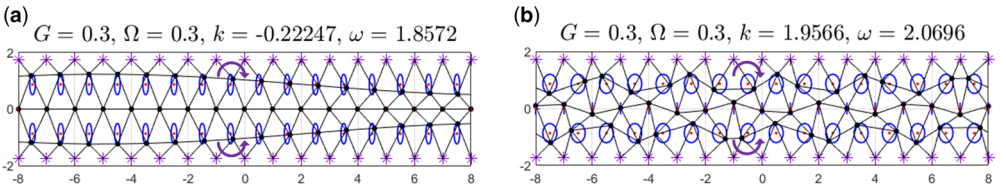

Fig. 8 Trajectories of the lattice strip nodal points for the normalised parameters $c = 1, l = 1, m = 1, G = 0.3$ and $\Omega = 0.3$, corresponding to standing waves with two different pairs (k, ω). The associated dispersion diagram is shown in Fig. 5, where the points $\mathcal{E}$ and $\mathcal{F}$ are linked to parts (a) and (b), respectively; (a) $(k, \omega) = (-0.22247, 1.8572)$ and (b) $(k, \omega) = (1.9566, 2.0696)$

3.2.3. Dirichlet strip: modes with zero vertical displacements of the central nodal points. In this section, we provide the analysis of the gyro-elastic Dirichlet strip modes which exhibit zero vertical displacements of the central nodal points (denoted by $j = 2$ in Fig. 3(b)). The conditions determining the motions of such nodal point trajectories are presented. In this case, we show that the horizontal displacements of the nodal points in the upper and lower layers of the Dirichlet strip follow the same direction, while their vertical displacements are in opposite directions.

Applying the conditions $(u_x^{(1)}, u_y^{(1)}) = (u_x^{(3)}, -u_y^{(3)})e^{-ikl}$ and $u_y^{(2)} = 0$ (see Section 3.1.2) and taking into account the analysis presented in Section 3.1.2, yields a simplified dispersion equation, which is a sixth-order polynomial in ω, of the form

$$\sigma_D^{(1)}(m, G, \Omega, k, \omega, c, l) = 0, \tag{3.16}$$

where $\sigma_D^{(1)}$ is defined in (3.13). The group velocity of the waveforms is given by implicitly differentiating (3.16) with respect to k, which yields the following:

$$\frac{d\omega}{dk} = \frac{\mathcal{F}_1}{\mathcal{G}_1}, \tag{3.17}$$

where

$$\mathcal{F}_1 = 2cl\sin(kl)m^2\omega^4 + l\left(4cm\cos(kl) - (\Omega^2 + 4G)m^2 - \frac{47cm}{4}\right)\sin(kl)c\omega^2$$
$$+\frac{l\sqrt{3}\cos(kl)\Omega c^2 m}{4}\omega + l\left(-\left(4Gm + \frac{21c}{2}\right)c\cos(kl) + 2G^2m^2 + \frac{47cGm}{4} + \frac{33c^2}{2}\right)\sin(kl)c, \tag{3.18}$$

and

$$\mathcal{G}_1 = 3m^3\omega^5 + m(8cm\cos(kl) - (2\Omega^2 + 6G)m^2 - 18cm)\omega^3$$
$$+m(4c^2\cos^2(kl) - 8\left(\left(\frac{\Omega^2}{4} + G\right)m + \frac{47c}{16}\right)c\cos(kl) + G(\Omega^2 + 3G)m^2 + 3(\Omega^2 + 6G)cm + 26c^2)\omega$$
$$-\frac{\sqrt{3}\Omega c^2 m\sin(kl)}{4}. \tag{3.19}$$

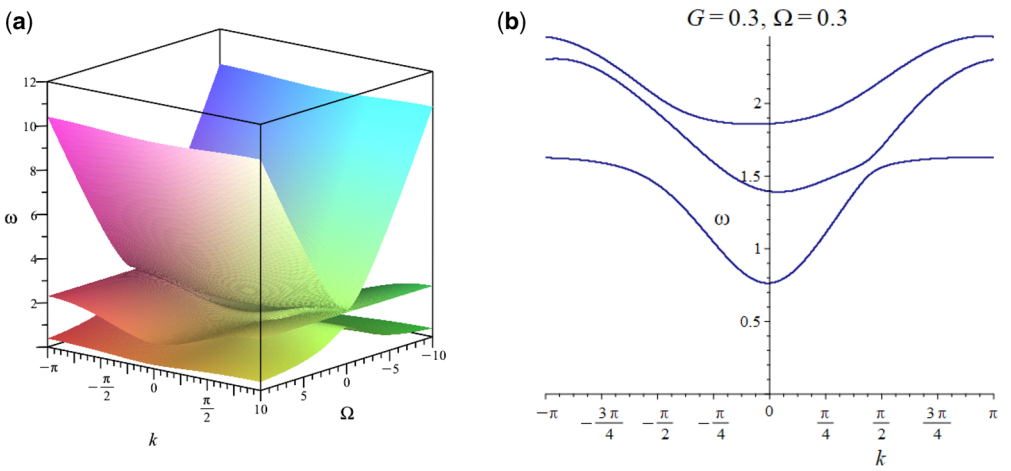

Fig. 9 (a) The graphs of ω as functions of k and Ω for the normalised parameter values $G = 0.3$, $m = 1, c = 1$ and $l = 1$, satisfying the dispersion Equation (3.16). The graphs represent a collection of dispersion curves for varying values of the gyricity parameter Ω. (b) Dispersion diagram for $\Omega = 0.3$ corresponding to three dispersion curves obtained by taking the vertical cross-section at $\Omega = 0.3$ of the surfaces shown in part (a). The same three dispersion curves are shown by the solid curves in Fig. 5

We note that when the group velocity (3.17) vanishes, there are standing modes of the Dirichlet strip with no vertical translations of the central nodal points. Conversely, a positive group velocity indicates a forward motion of the propagating waves, while a negative group velocity signifies a backward motion of the waveforms.

To illustrate the dynamic response of the chiral strip subjected to gravity for varying values of the gyricity parameter, we present the computations shown in Fig. 9. In Fig. 9(a), we have three surfaces corresponding to a set of three dispersion curves for varying values of Ω. There is also a zero-frequency stop band due to the prescribed Dirichlet boundary conditions (see Section 3.1). For $\Omega = 0.3$, there are three dispersion curves as shown in Fig. 9(b), which correspond to the curves obtained by taking the vertical cross-section of the surfaces presented in Fig. 9(a) at $\Omega = 0.3$. For large values of Ω, the chiral Dirichlet strip is dominated by gyroscopic forces, with the lower and central dispersion curves approaching $\omega = 0$ and the curve described by $\omega = \sqrt{(mG + 3c - 2c\cos(kl))/m}$, respectively, while the upper dispersion curve increases with Ω. This phenomenon is referred to as gyroscopic rigidity, where the gyroscopic effects become very dominant rendering the structure rigid. Additionally, we note that the dispersion Equation (3.16) is also dependent on the sign of the gyricity parameter Ω, and thus the surfaces presented in Fig. 9(a) are not symmetric relative to the $\Omega = 0$ plane—changing the sign of Ω is linked to the change in the orientation of motion of the nodal points. In the illustrative examples we consider the case of $\Omega \geq 0$ since the dispersion curves for $\{\Omega \geq 0, k \geq 0\}$ and $\{\Omega \geq 0, k \leq 0\}$ are equivalent to those for $\{\Omega \leq 0, k \leq 0\}$ and $\{\Omega \leq 0, k \geq 0\}$, respectively.

The set of three dispersion curves for varying values of the parameters G and Ω are shown in Fig. 10 for the symmetry-constrained system with no vertical motions of the central nodal points. In the absence of gyricity, that is $\Omega = 0$, the dispersion curves shown in Fig. 10(a) and (b) are symmetric

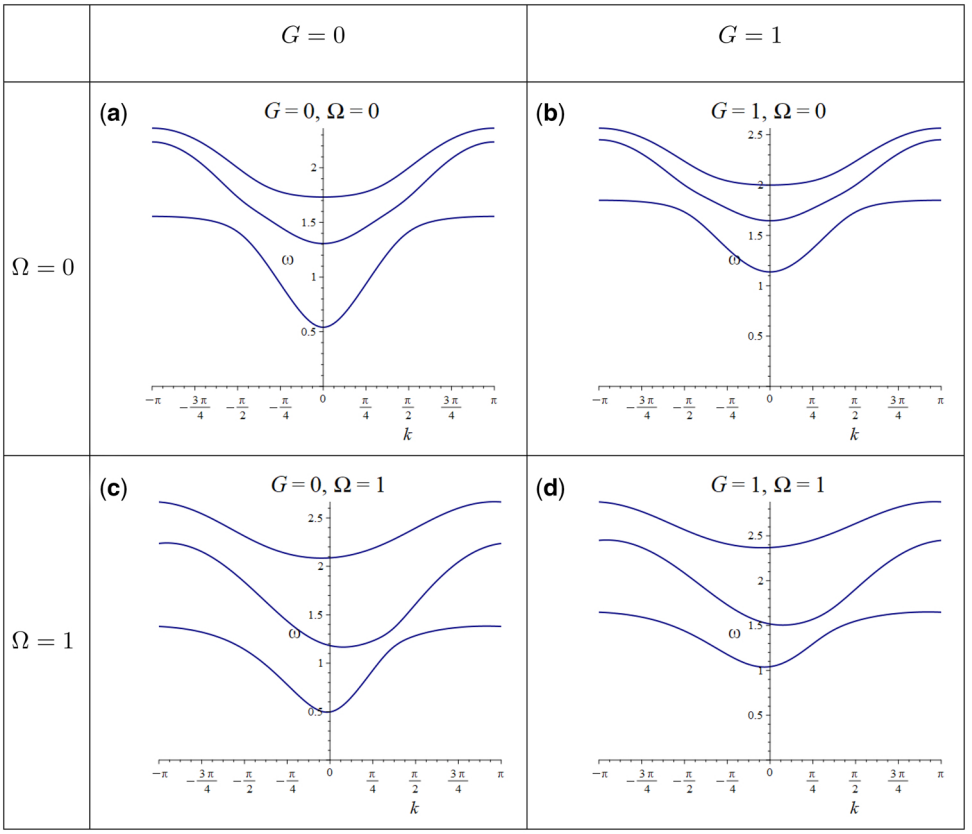

Fig. 10 Dispersion diagrams defined by the relation (3.16), illustrating the frequency ω against the wavenumber k, of the Dirichlet strip for a range of values of the gravity and gyricity parameters with $c = 1, l = 1$ and $m = 1$

relative to the ω-axis, and the signs of the group and phase velocities are the same. Conversely, additional wave characteristics are present when gyricity is introduced in the model as discussed in previous sections. Standing mode vibrations of the discrete lattice strip are also present for $\Omega > 0$, but unlike the $\Omega = 0$ case, they do not occur at $k = 0$ or $k = \pm\pi$. We also note that the dispersion diagram shown in Fig. 10(a) coincides with the three solid dispersion curves in Fig. 4(a). In particular, the three dashed curves in the dispersion diagrams illustrated in Fig. 4 correspond to the vibrations of the strip with zero horizontal displacements of the central nodal points and are analysed in the next section.

Examples of nodal point trajectories for the elastic chiral Dirichlet lattice strip with zero vertical displacements of the central nodal points, are presented in Fig. 11 for $G = 1$ and two different values of Ω. In the absence of gyricity, with $\Omega = 0$, the choices $k = -0.2$ and $k = 0.2$ result in elastic waves that propagate along the negative and positive x-direction, respectively, and for each case, the group and phase velocities have the same sign. The related dispersion diagrams are shown in Fig. 10(b)

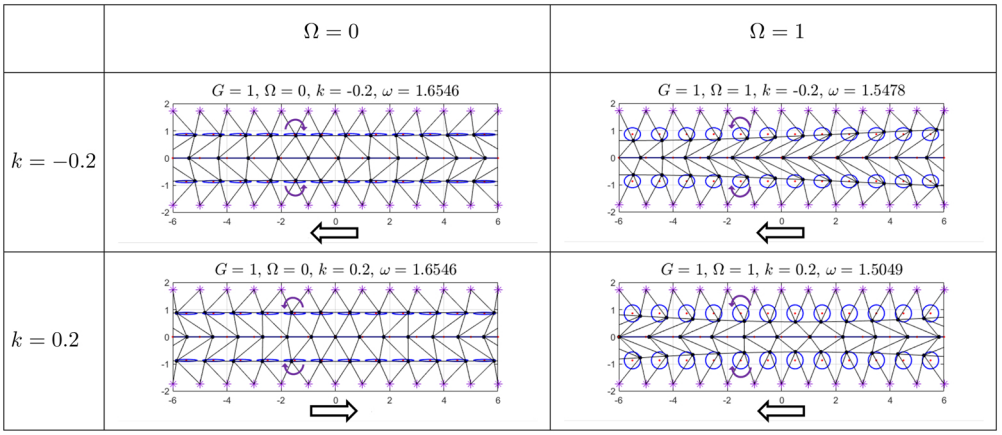

Fig. 11 Nodal point trajectories for the elastic Dirichlet strip for $\Omega = 0$ and $\Omega = 1$, with zero vertical displacements of the central nodal points. The normalised geometrical and physical parameter values of the model are $c = 1, l = 1$ and $m = 1$. The associated dispersion diagrams are shown in Fig. 10(b) and (d)

and (d), which illustrate the symmetric and asymmetric dispersion curves for $\Omega = 0$ and $\Omega \neq 0$, respectively. In particular, in Fig. 11 we also show the examples of the nodal point trajectories for $\Omega = 1$ with $k = -0.2$ and $k = 0.2$, where the group velocities are negative in both cases, while the phase velocities are negative when $k = -0.2$ and positive when $k = 0.2$. This characteristic of chiral wave phenomena can be exhibited in metamaterial structures, with applications to dynamic shielding, cloaking devices and vibration damping (see, for example, (**32**)). For a better visualisation of the nodal point trajectories connected to the propagating waveforms, we provide the illustrative videos in the electronic Supplementary Material.

3.2.4. Dirichlet strip: modes with zero horizontal displacements of the central nodal points. In this section, we analyse vibrations of the chiral Dirichlet lattice strip where the horizontal displacements of the central nodal points are zero, which differ from the motions of central nodal points with zero vertical displacements presented in Section 3.2.3. We show that the horizontal displacements of the nodal points in the upper and lower layers of the strip are in opposite directions, while their vertical motions are in the same direction (see also Section 3.1.1).

In this case, the motions of the nodal points satisfy the conditions $(u_x^{(1)}, u_y^{(1)}) = (-u_x^{(3)}, u_y^{(3)})e^{-ikl}$ and $u_x^{(2)} = 0$, associated with the dispersion equation

$$\sigma_D^{(2)}(m, G, \Omega, k, \omega, c, l) = 0, \tag{3.20}$$

where $\sigma_D^{(2)}$ is defined by (3.14). In a similar manner to Section 3.2.3, we can also implicitly differentiate (3.20) with respect to k and define the group velocity as follows

$$\frac{d\omega}{dk} = \frac{\mathcal{F}_2}{\mathcal{G}_2}, \tag{3.21}$$

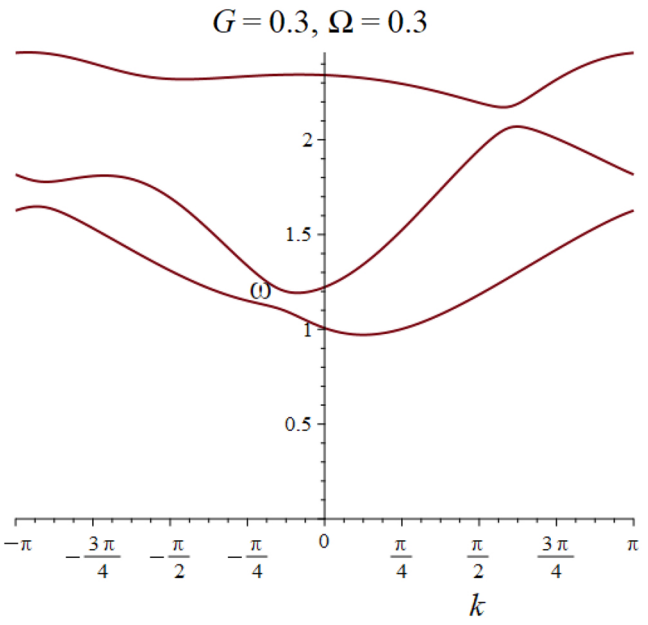

Fig. 12 Dispersion diagram of the Dirichlet strip for $G = 0.3$ and $\Omega = 0.3$, defined by (3.20), corresponding to the strip vibrations with zero horizontal displacements of the central nodal points. The same three dispersion curves coincide with the dashed dispersion curves in Fig. 5

where

$$\mathcal{F}_2 = c\sin(kl)m^2l\omega^4 - c\left(2Gm^2 + \frac{27cm}{4}\right)\sin(kl)l\omega^2 - \frac{3c^2\cos(kl)\sqrt{3}\Omega ml}{4}\omega + c\left(-\frac{9\cos(kl)c^2}{2} + G^2m^2 + \frac{27cGm}{4} + 9c^2\right)\sin(kl)l, \tag{3.22}$$

and

$$\mathcal{G}_2 = 3m^3\omega^5 + m(4cm\cos(kl) - (2\Omega^2 + 6G)m^2 - 18cm)\omega^3 + m\left(-4\left(Gm + \frac{27c}{8}\right)c\cos(kl) + G(\Omega^2 + 3G)m^2 + 3c(\Omega^2 + 6G)m + 24c^2\right)\omega + \frac{3\sqrt{3}\Omega c^2 m\sin(kl)}{4}. \tag{3.23}$$

The dispersion diagram illustrated in Fig. 12 corresponds to the chiral Dirichlet strip modes with solely vertical motions of the central nodal points; the chosen normalised parameter values are the same as in the example presented in Fig. 9(b). We note that in the limit when $\Omega \to \infty$, the two lower dispersion curves shown in Fig. 12 approach the curves described by $\omega = 0$ and $\omega = \sqrt{(mG + 3c)/m}$. Accordingly, the upper dispersion curve increases for increasing Ω.

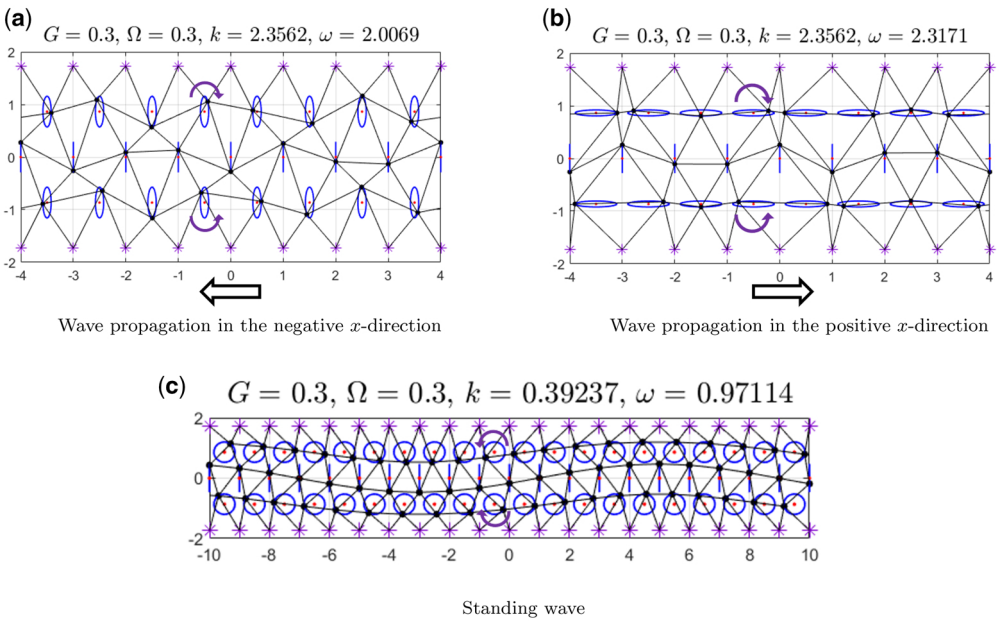

Fig. 13 Nodal point trajectories of the chiral strip with Dirichlet boundary conditions for $\Omega = 0.3$, $\Omega = 0.3$ and varying values of ω and k; (a) wave propagating in the negative x-direction with $(k,\omega) = (2.3562, 2.0069)$, (b) wave propagating in the positive x-direction with $(k,\omega) = (2.3562, 2.3171)$ and (c) standing wave with $(k,\omega) = (0.39237, 0.97114)$. For each example, the horizontal displacements of the central nodal points are zero. For the reader's convenience, we provide the videos of the above trajectories in the electronic supplementary material

Typical nodal point trajectories of the Dirichlet strip with zero horizontal displacements of the central nodal points are shown in Fig. 13 (see also Section 3.2.1). The presence of a gyroscopic action for the nodal points in the upper and lower layers of the strip result in a coupling of the transverse displacement components, leading to elliptical trajectories of such masses. The group velocity (see (3.21)) is negative for the example shown in Fig. 13(a) and positive for the oscillations displayed in Fig. 13(b), resulting in waveforms propagating, respectively, in the negative and positive x-directions along the strip. Conversely, a representative example of the nodal trajectories for a standing mode is shown in Fig. 13(c). For each example, the pair (k,ω) corresponds to a point on the dispersion diagram shown in Fig. 12.

3.3. *Chiral gravitational lattice strip with Neumann boundary conditions*

In this section, we present a chiral lattice strip system with prescribed Neumann boundary conditions, subjected to gravity, for which the equations of motion are derived. The dispersion properties of the structure are analysed, and we show that, in a similar manner to the chiral Dirichlet lattice strip presented in Section 3.1, waveforms with preferential directionality can also be exhibited in this type of lattice strip.

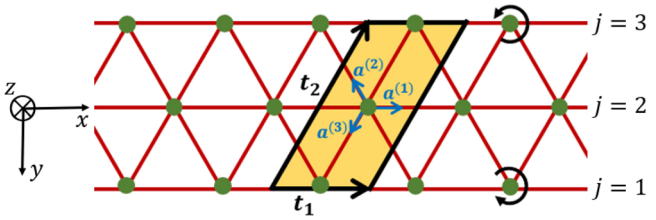

Fig. 14 Top view of the Neumann lattice strip consisting of gyropendulums, with nodal points connected by massless springs. The arrows indicate the choice of the lattice vectors for the elementary cell, defined by $\mathbf{t}_1$ and $\mathbf{t}_2$, and the unit vectors $\mathbf{a}^{(j)}$, $j = 1,2,3$, (see Section 3.3.1), together with the shaded region denoting the choice of the unit cell of the lattice. Similarly to the lattice strip with Dirichlet boundary conditions discussed in Section 3.1, here the lattice system is periodic along the x-axis, with its periodicity characterised by the lattice vector $\mathbf{t}_1$. The circular arrows represent the positive direction of spin of the gyroscopic spinners. The gravitational force acts in the positive z-direction

3.3.1. Equations of motion. We consider an infinite discrete lattice strip comprising of gyropendulums connected by springs with Neumann boundary conditions applied on the outer horizontal boundaries of the strip, as illustrated in Fig. 14. The lengths and stiffnesses of the springs, as well as the nodal point masses, are the same as in the model analysed in Section 3.1; only the boundary conditions and the geometries of the structure differ between the Dirichlet and Neumann strips. The problem assumptions and general parameter definitions used here are the same as in Section 3.1.

The elementary cell of the periodic structure is shown in Fig. 14, whose in-plane displacements are denoted by $\mathbf{u}^{(p,j)}$, for $j = 1,2,3$, where p is the integer index. Assuming time-harmonic displacements with the radian frequency ω, it follows that the equations of motion of the three nodal points are given by

$$-\tfrac{m\omega^2}{c}\mathbf{u}^{(p,1)} = (\mathbf{a}^{(1)}\cdot(\mathbf{u}^{(p+1,1)}-\mathbf{u}^{(p,1)}))\mathbf{a}^{(1)} + (\mathbf{a}^{(1)}\cdot(\mathbf{u}^{(p-1,1)}-\mathbf{u}^{(p,1)}))\mathbf{a}^{(1)}$$
$$+(\mathbf{a}^{(2)}\cdot(\mathbf{u}^{(p-1,2)}-\mathbf{u}^{(p,1)}))\mathbf{a}^{(2)} + (\mathbf{a}^{(3)}\cdot(\mathbf{u}^{(p,2)}-\mathbf{u}^{(p,1)}))\mathbf{a}^{(3)} + i\tfrac{m\Omega\omega}{c}\mathbf{R}\mathbf{u}^{(p,1)} - \tfrac{mG}{c}\mathbf{u}^{(p,1)}, \tag{3.24}$$

$$-\tfrac{m\omega^2}{c}\mathbf{u}^{(p,2)} = (\mathbf{a}^{(1)}\cdot(\mathbf{u}^{(p+1,2)}-\mathbf{u}^{(p,2)}))\mathbf{a}^{(1)} + (\mathbf{a}^{(1)}\cdot(\mathbf{u}^{(p-1,2)}-\mathbf{u}^{(p,2)}))\mathbf{a}^{(1)}$$
$$+(\mathbf{a}^{(2)}\cdot(\mathbf{u}^{(p-1,3)}-\mathbf{u}^{(p,2)}))\mathbf{a}^{(2)} + (\mathbf{a}^{(2)}\cdot(\mathbf{u}^{(p+1,1)}-\mathbf{u}^{(p,2)}))\mathbf{a}^{(2)}$$
$$+(\mathbf{a}^{(3)}\cdot(\mathbf{u}^{(p,1)}-\mathbf{u}^{(p,2)}))\mathbf{a}^{(3)} + (\mathbf{a}^{(3)}\cdot(\mathbf{u}^{(p,3)}-\mathbf{u}^{(p,2)}))\mathbf{a}^{(3)} - \tfrac{mG}{c}\mathbf{u}^{(p,2)}, \tag{3.25}$$

and

$$-\tfrac{m\omega^2}{c}\mathbf{u}^{(p,3)} = (\mathbf{a}^{(1)}\cdot(\mathbf{u}^{(p+1,3)}-\mathbf{u}^{(p,3)}))\mathbf{a}^{(1)} + (\mathbf{a}^{(1)}\cdot(\mathbf{u}^{(p-1,3)}-\mathbf{u}^{(p,3)}))\mathbf{a}^{(1)}$$
$$+(\mathbf{a}^{(2)}\cdot(\mathbf{u}^{(p+1,2)}-\mathbf{u}^{(p,3)}))\mathbf{a}^{(2)} + (\mathbf{a}^{(3)}\cdot(\mathbf{u}^{(p,2)}-\mathbf{u}^{(p,3)}))\mathbf{a}^{(3)} - i\tfrac{m\Omega\omega}{c}\mathbf{R}\mathbf{u}^{(p,3)} - \tfrac{mG}{c}\mathbf{u}^{(p,3)}, \tag{3.26}$$

where the parameters m, c, Ω and G are defined in Section 3.1.1. The vectors $\mathbf{a}^{(j)}$ for $j = 1,2,3$, are defined in (3.2), and the rotation matrix $\mathbf{R}$ is given by (3.7). The zero gyricity parameter is chosen for the nodal points along the central layer ($j = 2$ in Fig. 14) and the gravity parameter acts uniformly

at each nodal point. We also assume that the gyricities of the lower ($j = 1$) and upper ($j = 3$) layers of nodal points have the opposite sign but are the same in magnitude. Additional features of the non-gyroscopic Neumann strip subjected to gravity are discussed in Appendix D.

In a similar manner to the method provided in Section 3.1.1, by applying the Floquet–Bloch conditions (see (3.8)) into the system (3.24)–(3.26), we obtain the following system

$$[\mathbf{C}_N - \omega^2\mathbf{M} + \omega\mathbf{A}]\mathbf{W} = \mathbf{0}, \tag{3.27}$$

where

$$\mathbf{C}_N = -\begin{pmatrix} 2c[\cos(kl) - \frac{5}{4}] - Gm & 0 & \frac{c}{4}(e^{-ikl}+1) & \frac{c\sqrt{3}}{4}(-e^{-ikl}+1) & 0 & 0 \\ 0 & -\frac{3c}{2} - Gm & \frac{c\sqrt{3}}{4}(-e^{-ikl}+1) & \frac{3c}{4}(e^{-ikl}+1) & 0 & 0 \\ \frac{c}{4}(e^{ikl}+1) & \frac{c\sqrt{3}}{4}(-e^{ikl}+1) & 2c[\cos(kl) - \frac{3}{2}] - Gm & 0 & \frac{c}{4}(e^{-ikl}+1) & \frac{c\sqrt{3}}{4}(-e^{-ikl}+1) \\ \frac{c\sqrt{3}}{4}(-e^{ikl}+1) & \frac{3c}{4}(e^{ikl}+1) & 0 & -3c - Gm & \frac{c\sqrt{3}}{4}(-e^{-ikl}+1) & \frac{3c}{4}(e^{-ikl}+1) \\ 0 & 0 & \frac{c}{4}(e^{ikl}+1) & \frac{c\sqrt{3}}{4}(-e^{ikl}+1) & 2c[\cos(kl) - \frac{5}{4}] - Gm & 0 \\ 0 & 0 & \frac{c\sqrt{3}}{4}(-e^{ikl}+1) & \frac{3c}{4}(e^{ikl}+1) & 0 & -\frac{3c}{2} - Gm \end{pmatrix}, \tag{3.28}$$

and $\mathbf{M}$ and $\mathbf{A}$ are given in Section 3.1.2. The change in the prescribed conditions on the outer boundaries of the chiral lattice strip, from the Dirichlet boundary conditions used in Section 3.1 to the Neumann boundary conditions used here, results in different representations of the gravity-stiffness matrices. In the following analysis, we demonstrate how this change in boundary conditions affects the dispersion properties. In particular, we show that zero-frequency band gaps occur only due to the presence of gravitational forces when Neumann boundary conditions are prescribed. Conversely, zero-frequency stop bands exist independently of gravitational effects when Dirichlet boundary conditions are applied as discussed in Section 3.2. However, in both cases, the gravity parameter can be used to control the widths of the stop bands. We also show that the presence of gyricity leads to asymmetric dispersion diagrams for the chiral Neumann lattice strip, similar to those observed for the Dirichlet strip. This asymmetric feature of the dispersion curves is also present for the high-frequency inertia-gravity waves in the equatorial region as detailed in part 2.

3.3.2. Dispersion characteristics of the discrete strip with Neumann boundary conditions. To obtain non-trivial solutions of the system (3.27), the matrices $\mathbf{C}_N, \mathbf{M}$ and $\mathbf{A}$ must satisfy the condition

$$\det[\mathbf{C}_N - \omega^2\mathbf{M} + \omega\mathbf{A}] = \sigma_N^{(1)}(\Omega, G, m, \omega, k)\sigma_N^{(2)}(\Omega, G, m, \omega, k) = 0, \tag{3.29}$$

where

$$\begin{aligned} \sigma_N^{(1)}(m, G, \Omega, k, \omega) &= m^3\omega^6 - (-4c\cos(kl) + (\Omega^2 + 3G)m + 7c)m^2\omega^4 \\ &+ \Big(G\Omega^2m^2 - 2c\cos(kl)m\Omega^2 + 3G^2m^2 - 8c\cos(kl)Gm + 4c^2\cos^2(kl) + 3mc\Omega^2 \\ &+ 14Gcm - \frac{33c^2\cos(kl)}{2} + \frac{59c^2}{4}\Big)m\omega^2 - \frac{\sqrt{3}\Omega c^2m\omega\sin(kl)}{2} - 4G\cos^2(kl)c^2m \\ &- \frac{9\cos^2(kl)c^3}{2} + 4G^2\cos(kl)cm^2 + \frac{33G\cos(kl)c^2m}{2} \\ &+ \frac{27\cos(kl)c^3}{2} - G^3m^3 - 7G^2cm^2 - \frac{59Gc^2m}{4} - 9c^3, \end{aligned} \tag{3.30}$$

and

$$\begin{aligned}\sigma_N^{(2)}(m,G,\Omega,k,\omega) &= m^3\omega^6 - (-2c\cos(kl) + (\Omega^2+3G)m + 7c)m^2\omega^4 \\ &+\left(G\Omega^2m^2 + 3G^2m^2 - 4c\cos(kl)mG + 3mc\Omega^2 + 14Gcm - \frac{21c^2\cos(kl)}{2} + \frac{51c^2}{4}\right)m\omega^2 \\ &+\frac{3\sqrt{3}\Omega c^2m\omega\sin(kl)}{2} - \frac{9\cos^2(kl)c^3}{2} + 2G^2\cos(kl)cm^2 + \frac{21G\cos(kl)c^2m}{2} \\ &+9\cos(kl)c^3 - G^3m^3 - 7G^2cm^2 - \frac{51Gc^2m}{4} - \frac{9c^3}{2}.\end{aligned} \tag{3.31}$$

Similarly to the dispersion relation obtained for the Dirichlet lattice strip (see (3.1.2)), the dispersion equation for the Neumann lattice strip can also be written as a product of two sixth-order polynomials in ω as shown above. In particular, the dispersion curves for $\Omega < 0$ are equivalent to the dispersion curves for $\Omega > 0$ with a reflection in the vertical ω-axis and thus, without loss of generality, we only consider the latter case. The polynomial (3.30) is associated with the zero vertical displacements of the central nodal points (the $j = 2$ layer in Fig. 14), while the roots of the polynomial (3.31) correspond to the strip modes with zero horizontal displacements of the central nodal points. An analogous characteristic of the nodal point motions, in connection with the dispersion relation, also holds for the chiral Dirichlet strip. Furthermore, the nodal points in the lower ($j = 1$) and upper ($j = 3$) layers of the chiral Neumann strip move in opposite orientations.

In the illustrative examples, we take the normalised physical quantities $l = 1$, $c = 1$ and $m = 1$. Similarly to Section 3.2, the units of measurement will not be shown. Figures 15 and 16 illustrate the dispersion curves of the Neumann strip for different values of the gyricity and gravity parameters. There are six dispersion curves; the three dashed curves correspond to the roots of (3.30), while the three solid curves are characterised by the zeros of (3.31). It is apparent that there are intersection points of the dispersion curves, which correspond to the degeneracy points of the dispersion equation. These points also occur for the Dirichlet lattice strip as discussed in Appendix A. In both the Dirichlet and Neumann lattice strips, the gyroscopic effect introduced by the spinners allows for the chiral strip to support vortex-type waves. The nodal point trajectories of the Neumann strip corresponding to the points A, B, C, D, E and F in Fig. 16 are presented in the next section.

When gravitational forces are absent in the system ($G = 0$), there are no zero-frequency band gaps as shown in Fig. 15(a) and (c). When $G > 0$, a zero-frequency stop band is formed (see Fig. 15(b) and (d)). A similar feature was also noted in (1), where a chiral chain of gyropendulums subjected to gravity was considered. In addition, for $\Omega = 0$, the dispersion curves are symmetric relative to the ω-axis, whereas for $\Omega > 0$, they exhibit asymmetry. An analogous effect of the gyroscopic action was also observed for the dispersion diagrams of the Dirichlet strip (see Section 3.2). However, the presence of gravity leads to different properties of the dispersion curves due to the different boundary conditions on the lattice strip, especially in the low-frequency regime. Gyroscopic spinners also affect band-gap widths as well as the locations of the degeneracy points as illustrated in Figs 15(c), (d) and 16, where the gyricity parameter of the spinners are non-zero. In the limit when $\Omega \to \infty$, the two low-frequency dispersion curves tend to zero and the two intermediate dispersion curves

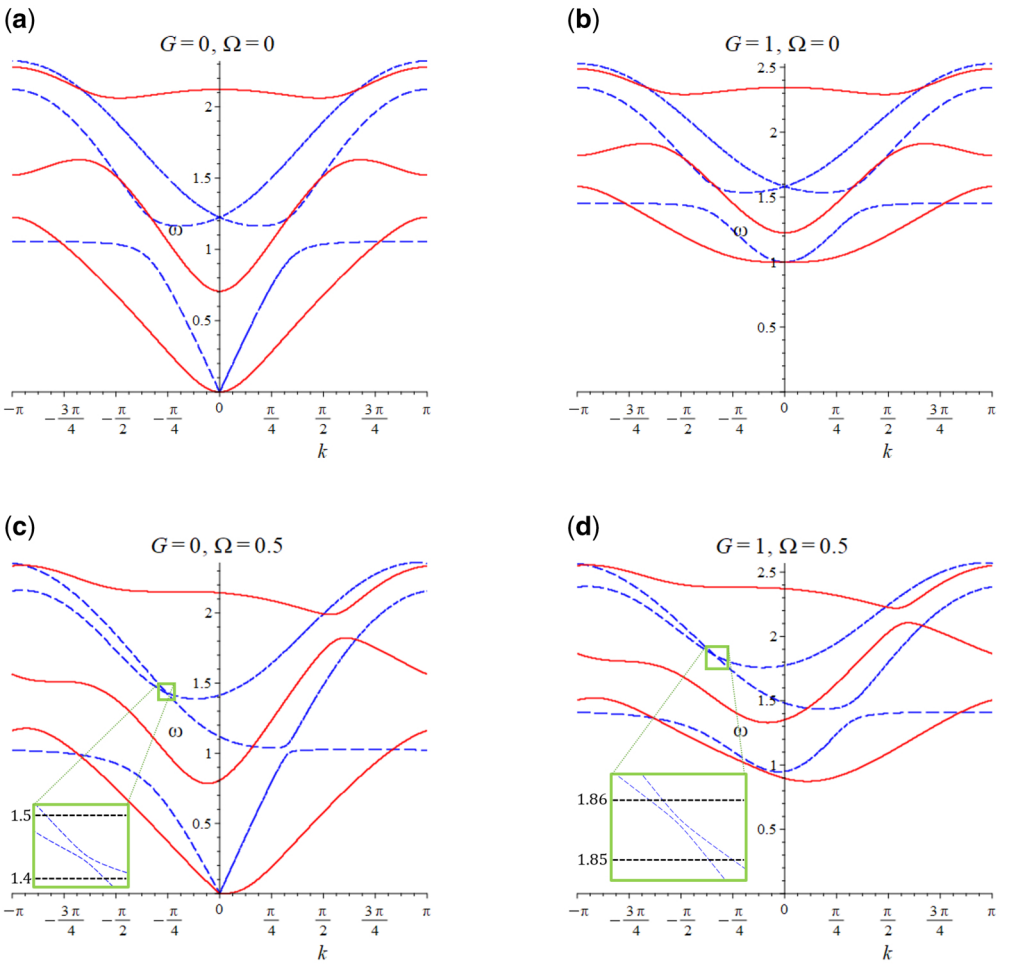

Fig. 15 Dispersion diagrams for the chiral gravitational lattice strip with Neumann boundary conditions; (a) $(G,\Omega) = (0,0)$, (b) $(G,\Omega) = (1,0)$, (c) $(G,\Omega) = (0,0.5)$ and (d) $(G,\Omega) = (1,0.5)$

approach the curves described by

$$\omega = \omega_1 = \sqrt{\frac{mG + 3c}{m}} = \text{const}, \ \omega = \omega_2(k) = \sqrt{\frac{mG + 3c - 2c\cos(kl)}{m}}. \tag{3.32}$$

Additionally, the two high-frequency dispersion curves increase for increasing Ω. The above frequencies, linked to gyroscopic rigidity, are the same as the limiting frequencies of the chiral Dirichlet strip (detailed in Section 3.2). This shows that gyroscopic rigidity is a property intrinsic to the rotating spinners.

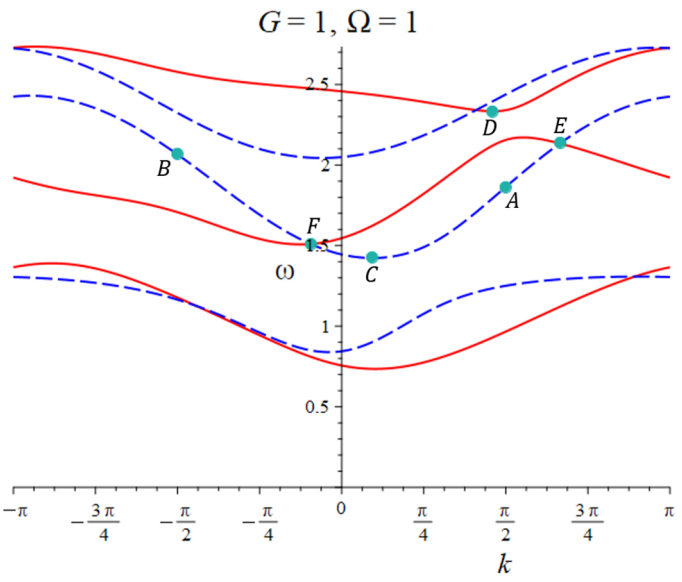

Fig. 16 Dispersion diagram for the Neumann strip with $G = 1$ and $\Omega = 1$. The nodal trajectories associated with the points A, B, C, D, E and F are discussed below

3.3.3. Dynamics of the chiral gravitational Neumann strip. In this section, we analyse the modes of an infinite chiral Neumann strip with the normalised parameter values $G = 1, \Omega = 1, c = 1, l = 1$ and $m = 1$, in connection with the propagating and standing waveforms along the structure.

Figure 17 shows the nodal points of the Neumann lattice strip for two different frequency values corresponding to the propagating waveforms. The nodal points in the upper and lower layers of the strip follow elliptical paths with the major axis aligned parallel to the strip, while the nodal points along the central layer move horizontally with no vertical components. Similar motions were also observed for the nodal points of the Dirichlet strip (see Section 3.2). Additionally, the group velocity is positive for the illustrative example shown in Fig. 17(a), resulting in waveforms propagating in the positive x-direction, whereas Fig. 17(b) displays waves propagating in the negative x-direction, where the group velocity is negative. We note that the vibration frequency is higher in Fig. 17(b) compared to Fig. 17(a) due to the asymmetry in the dispersion curves shown in Fig. 16. The examples in Fig. 17(a) and (b) are linked to the points A and B in Fig. 16.

Examples of trajectories for the chiral Neumann lattice strip corresponding to standing modes are shown in Fig. 18; these are associated with zero group velocities and zero net energy transfer along the strip. In both examples, the positive phase velocity corresponds to the phase of the wave moving in the positive x-direction. In Fig. 18, the trajectories of the nodal points in the upper and lower layers trace ellipses, while the central nodal points move either vertically or horizontally depending on the chosen vibration frequency. The frequencies and wavenumbers of the nodal point motions in Fig. 18(a) and (b) correspond to the points C and D in the dispersion diagram shown in Fig. 16. We also note that the eigenmodes of the finite three-dimensional belt shown in Fig. 2, exhibit similar motions to the standing modes of the Neumann strip illustrated in Fig. 18 for the same gravity and

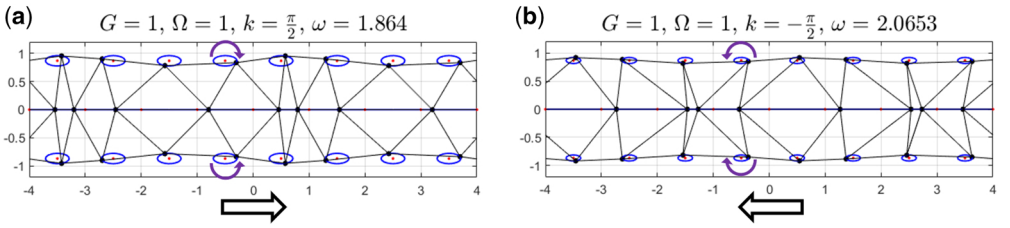

Fig. 17 Nodal point trajectories of the chiral gravitational lattice strip with prescribed Neumann boundary conditions. The circular arrows show the orientation of motion of the nodal points. The motions are associated with the points on the dispersion diagram shown in Fig. 16, denoted by *A* and *B* for parts (a) and (b), respectively; (a) wave propagating in the positive x-direction with $(k,\omega) = (\pi/2, 1.864)$ and (b) wave propagating in the negative x-direction with $(k,\omega) = (-\pi/2, 2.0653)$. The videos of the trajectories can be found in the electronic Supplementary Material

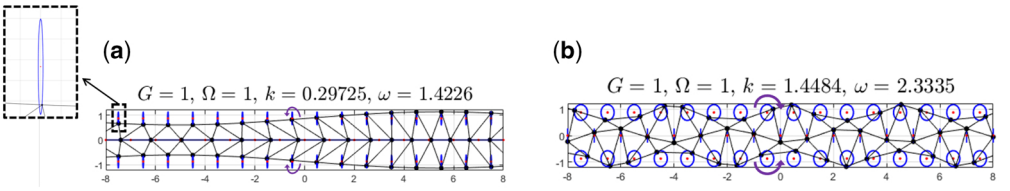

Fig. 18 Standing modes of the Neumann strip for the normalised parameter values $G = 1, \Omega = 1, m = 1, c = 1$ and $l = 1$ (see Section 3.3.1); (a) $(k,\omega) = (0.29725, 1.4226)$ and (b) $(k,\omega) = (1.4484, 2.3335)$

gyricity parameters. In particular, the nodal points on the central ring of the chiral belt also oscillate either horizontally or vertically, while the nodal points on the upper and lower rings trace elliptical trajectories with opposite orientations. Moreover, changes in frequency values affect the magnitudes and eccentricities of the ellipses, as well as the orientations of motion of the nodal points.

In Fig. 19, we present two examples of nodal point trajectories of the Neumann strip, with the frequencies and wavenumbers corresponding to the crossing points of the dispersion curves shown in Fig. 16. In the examples shown in Fig. 19, the trajectories of the nodal points are ellipses of varying sizes and orientations. Additionally, compared to the examples presented in Figs 17 and 18, there is no symmetry between the upper and lower nodal point trajectories shown in Fig. 19. This asymmetry was also observed in the nodal point trajectories of the Dirichlet lattice strip (see Fig. A1 in Appendix A). It is noted that although the central nodal points are characterised by zero gyricity, their trajectories are elliptical as displayed in Fig. 19 in contrast with the linear motions observed in Figs 17 and 18. The motions of the nodal points can be viewed through the illustrative videos included in the electronic Supplementary Material.

The examples presented in this section show a novel approach to modelling chiral elastic waveforms in a discrete strip with Neumann boundary conditions without perturbing the system, while taking into account the combined actions of gravitational and gyroscopic forces. The choices of frequency and wavenumber are important in describing the trajectories of the nodal points,

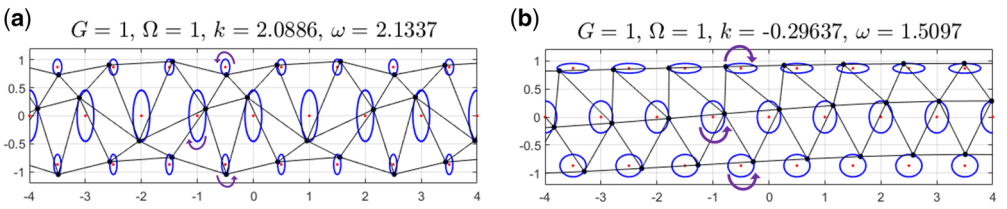

Fig. 19 Nodal point trajectories linked to the crossing points of the dispersion curves. The corresponding dispersion diagram is shown in Fig. 16, and the examples are associated with the points E and F for parts (a) and (b), respectively. (a) $(k,\omega) = (2.0886, 2.1337)$ and (b) $(k,\omega) = (-0.29637, 1.5097)$

influencing wave properties such as propagation speeds and the directionality of waveforms. The dispersion diagrams presented in Figs 15 and 16 determine how waveforms of different frequencies propagate through the discrete Neumann strip. Typical trajectories of the non-chiral Neumann strip are discussed in Appendix D, with an emphasis on standing and propagating waveforms.

4. Concluding remarks

Here, we have presented an analytical description of a chiral elastic lattice strip, of variable gyricity, subjected to gravity, with either Dirichlet or Neumann boundary conditions, demonstrating asymmetric waveforms. We have shown that the waveguides support elastic chiral vortex waves that can be controlled by adjusting the properties of the spinners and the gravity, which influence the dispersion of chiral waves.

This study also established a connection between the eigenmodes of a finite chiral belt and the standing waves within a two-dimensional chiral Neumann lattice strip. The modal study of the belt was presented in Section 2, which included the analysis of the typical eigenmodes of the structure. In Fig. 18, examples of standing modes for a Neumann lattice strip were presented for two different pairs (k,ω). In both models, there are zero net energy transfers and the direction of motion of the waveforms can be determined by the phase velocities for the chiral Neumann strip and by the mode shapes for the chiral belt.

The dynamics of the discrete lattice strip models discussed in this paper can be used as a simple analogy of the high-frequency inertia-gravity guided waves through the equatorial channel. The novel asymptotic analysis of equatorial and polar waves related to a rotating sphere is the subject of part 2, with an emphasis on the connections between Coriolis effects and gyroscopic forces. Part 2 investigates the continuum analogue of the discrete equatorial models considered here, focusing on the mathematical modelling of chiral wave dynamics subjected to gravity and gyroscopic forces in an equatorial region. The asymptotic analysis, presented in part 2, provides a set of boundary conditions for the equatorial band, in contrast with Matsuno's work (**25**), which used conditions of exponential decay at infinity.

Acknowledgments

A.K. gratefully acknowledges the financial support of the EPSRC through the Mathematics DTP grant EP/V52007X/1, project reference 2599756.

Author contributions

All the authors of the article, A.K., I.S.J., N.V.M and A.B.M., have contributed to the conception of the work, analysis, interpretation of data and writing the text of the article.

Supplementary data

Supplementary data are available online at *Quarterly Journal of Mechanics and Applied Mathematics*.

Data availability

All analytical data analysed during this study are included in this published paper. The illustrative videos are included in the electronic Supplementary Material provided for this paper.

Funding

Funding support for this article was provided by the EPSRC through the Mathematics DTP grant EP/V52007X/1, project reference 2599756.

Conflict of Interest

The authors declare that they have no conflicts of interest.

References

1. A. Kandiah, I. S. Jones, N. V. Movchan, A. B. Movchan. *et al*, Effect of gravity on the dispersion and wave localisation in gyroscopic elastic systems, *Mechanics of Heterogeneous Materials. Advanced Structured Materials*, Vol. **195** (eds H. Altenbach; Springer, Cham, Switzerland 2023) 219-274.
2. A. Bacigalupo, P. Badino, V. Diana and L. Gambarotta, Enhanced high-frequency continualization scheme for inertial beam-lattice metamaterials, *Int. J. Mech. Sci* **286** (2025) 109794.
3. V. Diana, A. Bacigalupo and L. Gambarotta, Thermodinamically-consistent dynamic continualization of block-lattice materials, *Int. J. Solids Struct* **262-263** (2023) 112050.
4. D. Bigoni, S. Guenneau, A. Movchan and M. Brun, Elastic metamaterials with inertial locally resonant structures: application to lensing and localization, *Phys. Rev. B* **87** (2013) 174303.
5. F. Hache, N. Challamel, I. Elishakoff and C. M. Wang, Comparison of nonlocal continualization schemes for lattice beams and plates, *Arch. Appl. Mech.* **87** (2017) 1105–1138.
6. G. Failla, A. Burlon and A. Russillo, A novel metamaterial multiple beam structure with internal local resonance, *Acta Mech.* **235** (2024) 5885–5903.
7. D. Bigoni and G. Noselli, Localized stress percolation through dry masonry walls. Part I-Experiments, *Eur. J. Mech. A/Solids* **29** (2010) 291–298.
8. D. Bigoni and G. Noselli, Localized stress percolation through dry masonry walls. Part II-Modelling, *Eur. J. Mech. A/Solids* **29** (2010) 299–307.
9. S. Chen and K. Bagi, Crosswise tensile resistance of masonry patterns due to contact friction, *Proc. R Soc. A.* **476** (2020) 20200439.

10. G. Failla, A. Marzani, A. Palermo, A. F. Russillo and D. Colquitt, Current developments in elastic and acoustic metamaterials science, *Philos. Trans. A Math. Phys. Eng. Sci.* **382** (2024) 20230369.
11. P. Jiao, J. Mueller, J. Raney, X. Zheng and A. Alavi, Mechanical metamaterials and beyond, *Nat. Commun.* **14** (2023) 6004.
12. R. Bollineni, M. Ahmed, S. Shahab and R. Mirzaeifar, Nacre-like block lattice metamaterials with targeted phononic band gap and mechanical properties, *J. Mech. Behav. Biomed. Mater.* **154** (2024) 106511.
13. J. Chapuis, T. Lumpe and K. Shea, Mechanical properties of topological metamaterials, *Extreme Mech. Lett*. **55** (2022) 101835.
14. S. Gonella, Symmetry of the phononic landscape of twisted kagome lattices across the duality boundary, *Phys. Rev. B.* **102** (2020) 140301.
15. G. Carta, I. Jones, N. Movchan and A. Movchan, Wave polarization and dynamic degeneracy in a chiral elastic lattice, *Proc. Math. Phys. Eng. Sci.* **475** (2019) 20190313.
16. G. Carta, D. Colquitt, A. Movchan, N. Movchan and I. Jones, One-way interfacial waves in a flexural plate with chiral double resonators, *Philos. Trans. A Math. Phys. Eng. Sci.* **378** (2020) 20190350.
17. G. Carta, D. Colquitt, A. Movchan, N. Movchan and I. Jones, Chiral flexural waves in structured plates: directional localisation and control, *J. Mech. Phys. Solids* **137** (2020) 103866.
18. M. Garau, G. Carta, M. Nieves, I. Jones, N. Movchan and A. Movchan, Interfacial waveforms in chiral lattices with gyroscopic spinners, *Proc. Math. Phys. Eng. Sci.* **474** (2018) 20180132.
19. G. Carta, I. Jones, N. Movchan, A. Movchan and M. Nieves, Deflecting elastic prism and unidirectional localisation for waves in chiral elastic systems, *Sci. Rep.* **7** (2017) 26.
20. E. Lorenz, The nature and theory of the general circulation of the atmosphere, *WMO* (1967) 161.
21. G. V. Hadley, Concerning the cause of the general trade-winds, *Philos. Trans. R. Soc*. **39** (1735) 58–62.
22. B. Wang, Kelvin waves, *Encycl. Atmos. Sci*. (2002) 1062–1068.
23. P. Delplace, J. Marston and A. Venaille, Topological origin of equatorial waves, *Science* **358** (2017) 1075–1077.
24. M. Lighthill, Dynamic response of the Indian Ocean to onset of the southwest monsoon, *Philos. Trans. R. Soc. A* **265** (1969) 45–92.
25. T. Matsuno, Quasi-geostrophic motions in the equatorial area, *J Meteorol. Soc. Jpn*. **44** (1966) 25–43.
26. P. LeBlond and L. Mysak, *Waves in the Ocean*. (Elsevier, Amsterdam, The Netherlands 1978)
27. A. Gill, *Atmosphere-Ocean Dynamics*. (Academic Press, London, UK 1982)
28. G. Coriolis, Sur les équations du mouvement relatif des systèmes de corps, *J. École Polytechnique, Paris* **5** (1835) 142.
29. C. Abbe, The mechanics of the Earth's atmosphere, *Smithson. Misc. Collect* **51** (Washington D.C., USA 1910).
30. G. Carta, M. Brun, A. Movchan, N. Movchan and I. Jones, Dispersion properties of vortex-type monatomic lattices, *Int. J. Solids. Struct*. **51** (2014) 2213–2225.
31. I. Jones, N. Movchan and A. Movchan, Two-dimensional waves in a chiral elastic chain: Dynamic green's matrices and localised defect modes, *Q. J. Mech. Appl. Math*. **73** (2021) 305–328.

32. M. Brun, I. Jones and A. Movchan, Vortex-type elastic structured media and dynamic shielding, *Proc. R Soc. A.* **468** (2012) 3027–3046.
33. I. Jones, N. Movchan and A. Movchan, Chiral waves in structured elastic systems: dynamics of a meta-waveguide, *Q. J. Mech. Appl. Math.* **75** (2022) 63–89.
34. A. Kandiah, I. Jones, N. Movchan and A. Movchan, Controlling the motion of gravitational spinners and waves in chiral waveguides, *Sci. Rep.* **14** (2024) 1203.
35. I. Jones, N. Movchan and A. Movchan, Gravity-induced dispersion in a chiral waveguide: transient regimes and imperfect temporal interfaces, *Proc. R Soc. A.* **479** (2023) 20230338.
36. J. Hou and W. Chen, Hidden symmetry and protection of dirac points on the honeycomb lattice, *Sci. Rep.* **5** (2015) 17571.
37. W. He and C. Chan, The emergence of dirac points in photonic crystals with mirror symmetry, *Sci. Rep.* **5** (2015) 8186.

Appendix A. Dispersion degeneracies of the Dirichlet lattice strip

The dispersion degeneracies of the Dirichlet lattice strip introduced in Section 3.1, linked to the crossing and touching points of the dispersion curves, are discussed in this appendix. At these points, there are repeated roots of the dispersion equation. The crossing points are identified by the intersection of two dispersion curves, while the touching points correspond to the tangents of two dispersion curves with equivalent group velocities at the touching point. This feature is inherent to the Dirichlet lattice strip and does not depend on the gravitational and gyroscopic effects. However, the properties of the spinners and magnitude of the gravity parameter can be used to alter the behaviour of the band structure in the vicinity of the degeneracy points. At such points on the dispersion diagram, the oscillations of the nodal points in the strip do not exhibit symmetric modes relative to the central horizontal layer, and the central nodal points can display elliptical trajectories. In the absence of gravity, the ability to control the locations of crossing points using gyroscopic spinners in a lattice system has been studied in (**18**). The presence of crossing points is also related to the symmetries of the medium (see, for example, (**36, 37**)).

In the absence of gyroscopic forces, there are three touching points and two crossing points for both $k > 0$ and $k < 0$. In this case, the points of degeneracy occur at the same k values independently of the gravity parameter G (see Fig. 4(a) and (b) in the main text). For $\Omega = 0$, the set of dispersion curves are symmetric with respect to the ω-axis, so that if there is a crossing (touching) point at (k_*, ω_*), then there is also another distinct crossing (touching) point at $(-k_*, \omega_*)$. When $\Omega = 0$, the touching points occur at $k = \pi/2$ and $k = \pi$, while the crossing points are observed at $k = \pi/4$ and $k = 3\pi/4$. The introduction of gyricity leads to asymmetric dispersion curves relative to the frequency axis, and a change in the number of crossing and touching points.

At the touching points of the dispersion curves with $\Omega = 0$, the trajectories of the nodal points can follow linear motions due to the absence of gyroscopic forces. The touching point at $kl = \pi/2$ occurs at the frequency $\omega = \sqrt{(mG + 3c)/m}$, while the two touching points at $kl = \pi$ correspond to the frequency values

$$\omega = \sqrt{\frac{2mG + 8c - c\sqrt{10}}{2m}}, \quad \omega = \sqrt{\frac{2mG + 8c + c\sqrt{10}}{2m}}. \tag{A.1}$$

The crossing points of the dispersion curves for the non-gyroscopic Dirichlet strip, for $k \geq 0$, occur at $kl = \pi/4$ and $kl = 3\pi/4$ with the frequencies, respectively, given by

$$\omega = \sqrt{\frac{2mG - 3c\sqrt{2} + 6c}{2m}}, \quad \omega = \sqrt{\frac{2mG + 3c\sqrt{2} + 6c}{2m}}. \tag{A.2}$$

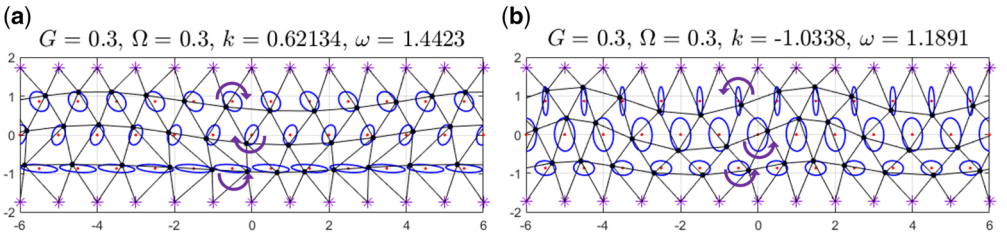

Fig. A1 Trajectories of the nodal points associated with the crossing points of the dispersion curves shown in Fig. 5. The normalised parameter values are $\Omega = 0.3$, $G = 0.3, m = 1, c = 1$ and $l = 1$; (a) $(k,\omega) = (0.62134, 1.4423)$ and (b) $(k,\omega) = (-1.0338, 1.1891)$. The trajectories of all nodal points are elliptical. The circular arrows show the orientation of motion of the nodal points

The touching and crossing points of the dispersion curves for $k < 0$ and $\Omega = 0$ occur at the same frequencies shown above for the corresponding negative values of k.

In Fig. A1, we present illustrative examples of the nodal trajectories in the chiral Dirichlet strip linked to the crossing points of the dispersion curves shown in Fig. 5 (denoted by the points $\mathcal{G}$ and $\mathcal{H}$ for Fig. A1(a) and (b), respectively). In both examples, the central nodal points move in an elliptical motion, which differ from the horizontal or vertical motions described in Sections 3.2.1 and 3.2.2. This motion of the central nodal points corresponds to a linear combination of two modes associated with their horizontal and vertical components. Figure A1(a) displays the elliptical trajectories of the nodal points with $\omega = 1.4423$ rad/s, where the upper and central nodal points move in a clockwise orientation, while the lower nodal points move counterclockwise. The motion of the chiral Dirichlet strip for a different crossing point corresponding to the frequency $\omega = 1.1891$ rad/s is shown in Fig. A1(b). In this case, the elliptical trajectories of all nodal points follow a counterclockwise orientation. In both examples, the major axes of the ellipses traced by the nodal points are neither parallel nor perpendicular to the strip. We also note that the phase velocity is positive in the example presented in Fig. A1(a) and negative in the example shown in Fig. A1(b).

Appendix B. Active two-dimensional chiral strip with Dirichlet-type boundary conditions

In this appendix, we investigate the dynamics of a lattice strip with Dirichlet boundary conditions (see Section 3.1) for an active system. The term active refers to the gyricity being proportional to the frequency of the vibrations, where the gyricity is adjusted according to the ambient system. Mathematically, we enforce an active system by choosing $\Omega = \alpha\omega$, where α is the gyricity control parameter that ensures the compatibility of the gyroscopic spinner with the time-harmonic strip vibrations (see, for example, (**32**)). The latter choice leads to a dispersion equation similar to that of (3.12) in the main text, but each polynomial in ω can now be written as a product of two cubic polynomials in ω^2 as detailed below. The characteristic motions of the central nodal point trajectories for the active Dirichlet strip are similar to the passive (non-active) system discussed in Section 3.1, but the dispersion properties change according to the choice of α.

For the active system, the dispersion relation for the Dirichlet strip takes the form

$$\det[\mathbf{C}_D - \omega^2(\mathbf{M} - \mathbf{A}_\alpha)] = 0, \tag{B.1}$$

where the matrices $\mathbf{C}_D$ and $\mathbf{M}$ are defined in Section 3.1.2 and

$$\mathbf{A}_\alpha = i\begin{pmatrix} 0 & -m\alpha & 0 & 0 & 0 & 0 \\ m\alpha & 0 & 0 & 0 & 0 & 0 \\ 0 & 0 & 0 & 0 & 0 & 0 \\ 0 & 0 & 0 & 0 & 0 & 0 \\ 0 & 0 & 0 & 0 & 0 & m\alpha \\ 0 & 0 & 0 & 0 & -m\alpha & 0 \end{pmatrix}. \tag{B.2}$$

The dispersion relation (B.1) can be written as follows (see (3.13) and (3.14)):

$$\sigma_D^{(1)}(m,G,\Omega,k,\omega,c,l)\sigma_D^{(2)}(m,G,\Omega,k,\omega,c,l)|_{\Omega=\alpha\omega} = 0, \tag{B.3}$$

where

$$\begin{aligned} \sigma_D^{(1)}(m,G,\Omega,k,\omega,c,l)|_{\Omega=\alpha\omega} &= m^3(1-\alpha^2)\omega^6 + m^2(mG\alpha^2 - 2c\cos(kl)\alpha^2 \\ &+3c\alpha^2 - 3mG + 4c\cos(kl) - 9c)\omega^4 \\ +\frac{m}{2}(-\sqrt{3}\sin(kl)\alpha c^2 &+ 6G^2m^2 - 16Gcm\cos(kl) + 8c^2\cos(kl)^2 + 36cmG - 47\cos(kl)c^2 + 52c^2)\omega^2 \\ -4mG\cos(kl)^2c^2 - \frac{21}{2}\cos(kl)^2c^3 &+ 4G^2\cos(kl)cm^2 + \frac{47}{2}G\cos(kl)c^2m + 33\cos(kl)c^3 \\ -G^3m^3 - 9G^2cm^2 &- 26Gc^2m - 24c^3, \end{aligned} \tag{B.4}$$

and

$$\begin{aligned} \sigma_D^{(2)}(m,G,\Omega,k,\omega,c,l)|_{\Omega=\alpha\omega} &= m^3(1-\alpha^2)\omega^6 + m^2(mG\alpha^2 + 3c\alpha^2 - 3mG + 2c\cos(kl) - 9c)\omega^4 \\ +\frac{m}{2}(3\sqrt{3}\sin(kl)\alpha c^2 &+ 6G^2m^2 - 8G\cos(kl)cm + 36Gcm - 27\cos(kl)c^2 + 48c^2)\omega^2 \\ -\frac{9}{2}\cos(kl)^2c^3 + 2G^2\cos(kl)cm^2 &+ \frac{27}{2}G\cos(kl)c^2m + 18\cos(kl)c^3 - G^3m^3 - 9G^2cm^2 - 24Gc^2m - 18c^3. \end{aligned} \tag{B.5}$$

To simplify our analysis, we take the normalised physical quantities $c = 1, l = 1$ and $m = 1$. Then, the leading coefficient of the dispersion relation (B.3) is $(1-\alpha^2)^2$, that is the coefficient of ω^{12}, which allows for a description of the dispersion properties by comparing the spinner constant α against the unit value.

When $\alpha < 1$, the Equation (B.1) yields six solutions for ω, resulting in six dispersion curves. Conversely, when $\alpha \geq 1$, the dispersion equation degenerates, yielding four positive solutions for ω. The dispersion curves yield the frequencies and wavenumbers corresponding to the elliptical trajectories of the nodal points in the upper and lower layers of the strip, and to the horizontal or vertical motions of the central nodal points.

Illustrative examples of the dispersion diagrams for varying values of the spinner constant α, linked to the active chiral system, are presented in Fig. B1 for the gravity parameter $G = 1$. We note that, similarly to the passive system discussed in the main text, the gravity parameter can be used to modulate the zero-frequency band gap of the active Dirichlet strip, while the presence of gyricity breaks the symmetry of the dispersion curves relative to the frequency axis. When $\alpha = 0$ (no spinners are attached to the strip), there are generally six frequency values ω for a fixed wavenumber k, which may degenerate to frequencies of a higher multiplicity

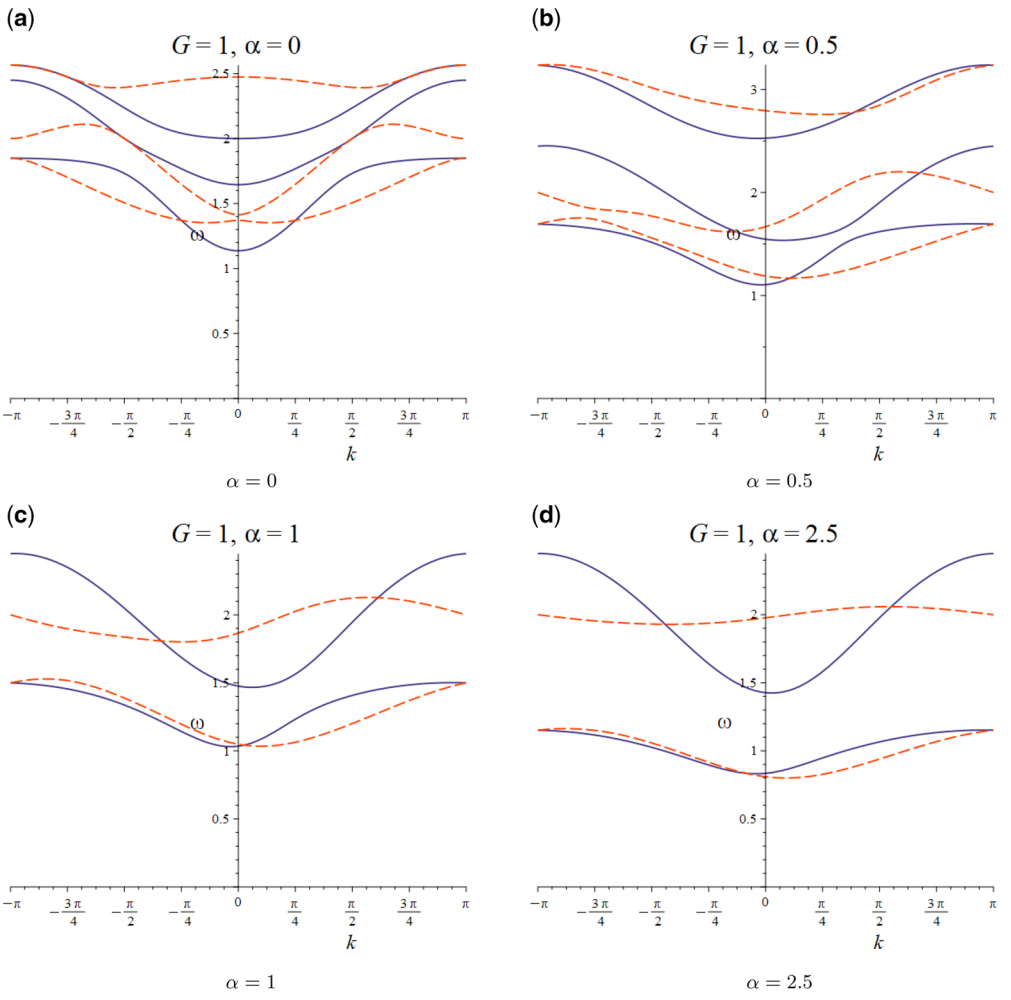

Fig. B1 Dispersion diagrams for the active Dirichlet lattice strip for various values of the gyricity control parameter α. The gravity parameter is chosen as $G = 1$, and the physical parameter values, which are normalised by the system's natural units, are chosen as $c = 1, l = 1$ and $m = 1$. The solid and dashed dispersion curves (defined by the roots of (B.4) and (B.5)) correspond to the trajectories of the central nodal points with zero vertical and zero horizontal displacements, respectively; (a) $\alpha = 0$, (b) $\alpha = 0.5$, (c) $\alpha = 1$ and (d) $\alpha = 2.5$

corresponding to crossing or touching points of the dispersion curves (see also Appendix A). In this case, the degeneracy points coincide with the degeneracy points of the dispersion curves for the passive Dirichlet strip with zero gyricity. The dispersion degeneracies of the passive Dirichlet lattice strip are discussed in Appendix A, which also includes examples of the corresponding nodal point trajectories. When $0 < \alpha < 1$, the dispersion curves are asymmetric relative to the ω-axis, as shown in Fig. B1(b). When $\alpha \geq 1$, there are four dispersion curves as illustrated in Fig. B1(c) and (d). In the limit as $\alpha \to \infty$, the two lower dispersion curves tend towards

$\omega = 0$ for any wavenumber k, while the two upper dispersion curves approach the curves described by

$$\omega = \omega_1 = \sqrt{\frac{mG + 3c}{m}} = \text{const}, \ \omega = \omega_2(k) = \sqrt{\frac{mG + 3c - 2c\cos(kl)}{m}}. \tag{B.6}$$

Increasing α results in an additional finite-width stop band and a change in the number of crossing and touching points compared to $\alpha = 0$.

The trajectories of the nodal points are comparable in behaviour between the active and passive Dirichlet lattice strips, while the dispersion characteristics differ as detailed above. In particular, for $\alpha < 1$, the solid and dashed dispersion curves (see Fig. B1) for the active Dirichlet strip are associated with zero vertical and zero horizontal displacements of the central nodal points, respectively.

Appendix C. Nodal trajectories of the dirichlet strip

This appendix includes auxiliary derivations related to the nodal point trajectories of the Dirichlet lattice strip of Section 3.1.

C.1. Displacements of the nodal points corresponding to the dispersion relation (3.16)

The dispersion Equation (3.16) for the Dirichlet strip, given in Section 3.2, describes the connection between the frequency ω and wavenumber k of the waveforms along the infinite chiral lattice strip. When (3.16) is satisfied, the nodal points in the central layer (denoted by $j = 2$ in Fig. 3(b) of the main text) move only in the horizontal direction, and the nodal points in the lower ($j = 1$) and upper ($j = 3$) layers follow elliptical trajectories of opposite orientations. In this case, the time-harmonic transverse displacements of the nodal points along the j-th horizontal strip, for $j = 1,2,3$, are given by (see Section 3.1)

$$\mathbf{u}_j^{(n)} = \text{Re}\big(\mathbf{U}_j e^{i(knl-\omega t)}\big), \tag{C.1}$$

where the displacement amplitude eigenvector $\mathbf{U}_j$ has the components

$$\mathbf{U}_1 = \frac{e^{-ikl}}{\mathfrak{a}_1 + i\mathfrak{a}_2}(i\mathfrak{A}, -\mathfrak{B})^T, \quad \mathbf{U}_2 = (1,0)^T, \quad \mathbf{U}_3 = \frac{1}{\mathfrak{a}_1 + i\mathfrak{a}_2}(i\mathfrak{A}, \mathfrak{B})^T, \tag{C.2}$$

where

$$\mathfrak{A} = 2m^2\omega^4 - 4m(Gm - c\cos(kl) + 3c)\omega^2 - 4(mG + \frac{21c}{8})c\cos(kl) + 2G^2m^2 + 12cGm + \frac{33c^2}{2},$$

$$\mathfrak{B} = 2m^2\Omega\omega^3 + m\Omega(4c\cos(kl) - 2(Gm + 3c))\omega + \frac{\sqrt{3}c^2\sin(kl)}{2},$$

$$\mathfrak{a}_1 = -cm\sin(kl)\omega^2 + \sqrt{3}m\Omega c(\cos(kl) - 1)\omega + c(mG + 3c)\sin(kl),$$

$$\mathfrak{a}_2 = -mc(\cos(kl) + 1)\omega^2 - c\sqrt{3}m\Omega\sin(kl)\omega + c(mG + 3c)(\cos(kl) + 1).$$

We note that the vertical displacement component of the central nodal points vanishes as shown by the representation of $\mathbf{U}_2$ in (C.2). The components of the amplitude eigenvectors for the remaining nodal points are complex, resulting in elliptical trajectories of the nodal points in the lower ($j = 1$) and upper ($j = 3$) layers of the Dirichlet strip. These trajectories are identical but are traced in opposite directions.

The equations of the trajectories of the central nodal points are

$$x_2^{(n)} = \cos(knl - \omega t), \quad y_2^{(n)} = 0, \tag{C.3}$$

and the trajectories of the nodal points in the lower ($j = 1$) and upper ($j = 3$) layers of the Dirichlet strip are given respectively by

$$\left(\frac{\sqrt{\mathfrak{a}_1^2 + \mathfrak{a}_2^2}}{\mathfrak{A}} x_1^{(n)}\right)^2 + \left(\frac{\sqrt{\mathfrak{a}_1^2 + \mathfrak{a}_2^2}}{\mathfrak{B}} y_1^{(n)}\right)^2 = 1, \quad \left(\frac{\sqrt{\mathfrak{a}_1^2 + \mathfrak{a}_2^2}}{\mathfrak{A}} x_3^{(n)}\right)^2 + \left(\frac{\sqrt{\mathfrak{a}_1^2 + \mathfrak{a}_2^2}}{\mathfrak{B}} y_3^{(n)}\right)^2 = 1, \tag{C.4}$$

where $x_j^{(n)}$ and $y_j^{(n)}$ are the local coordinates associated with the elliptical trajectory of the n-th node on the j-th layer, for $j = 1$ and $j = 3$. The local origin corresponds to the equilibrium position of node n for each layer. The $x_j^{(n)}$ and $y_j^{(n)}$ axes are parallel and perpendicular to the j-th layer, respectively. Thus, the trajectories of the nodal points of the Dirichlet lattice strip along $j = 1$ and $j = 3$ (see Fig. 3(b)) are elliptical with axes aligned parallel and perpendicular to the j-th layer.

C.2. Displacements of the nodal points corresponding to the dispersion relation (3.20)

When the dispersion Equation (3.20) is satisfied, the nodal points along the central layer ($j = 2$) move only in the vertical direction, which differs from the horizontal motions discussed above, whereas the nodal points in the upper and lower layers follow elliptical trajectories. In this case, the vibrations of the Dirichlet strip can be expressed in a similar time-harmonic form as (C.1), with the displacement amplitude eigenvector components represented as follows

$$\mathbf{U}_1 = \frac{e^{-ikl}}{\mathfrak{c}_1 + i\mathfrak{c}_2}(-i\mathfrak{C}, \mathfrak{D})^T, \quad \mathbf{U}_2 = (0, 1)^T, \quad \mathbf{U}_3 = \frac{1}{\mathfrak{c}_1 + i\mathfrak{c}_2}(i\mathfrak{C}, \mathfrak{D})^T, \tag{C.5}$$

where

$$\mathfrak{C} = -2m^2\Omega\omega^3 + 2(Gm + 3c)\Omega m\omega + \frac{3\sqrt{3}c^2\sin(kl)}{2},$$

$$\mathfrak{D} = -2m^2\omega^4 + 4m(Gm - c\cos(kl) + 3c)\omega^2 + 4\left(Gm + \frac{21c}{8}\right)c\cos(kl) - 2G^2m^2 - 12cGm - \frac{33c^2}{2},$$

$$\mathfrak{c}_1 = 3mc(\cos(kl) + 1)\omega^2 - c\sqrt{3}m\Omega\sin(kl)\omega - 3c(-2c\cos(kl)^2 + (Gm + c)\cos(kl) + Gm + 3c),$$

$$\mathfrak{c}_2 = -3cm\sin(kl)\omega^2 - \sqrt{3}m\Omega c(\cos(kl) - 1)\omega + 3c(Gm - 2\cos(kl)c + 3c)\sin(kl).$$

Then, the central nodal point trajectories are described by

$$x_2^{(n)} = 0, \quad y_2^{(n)} = \cos(knl - \omega t), \tag{C.6}$$

while the equations governing the motion of the nodal points in the lower ($j = 1$) and upper ($j = 3$) layers of the Dirichlet strip are, respectively, given by

$$\left(\frac{\sqrt{\mathfrak{c}_1^2 + \mathfrak{c}_2^2}}{\mathfrak{C}} x_1^{(n)}\right)^2 + \left(\frac{\sqrt{\mathfrak{c}_1^2 + \mathfrak{c}_2^2}}{\mathfrak{D}} y_1^{(n)}\right)^2 = 1, \quad \left(\frac{\sqrt{\mathfrak{c}_1^2 + \mathfrak{c}_2^2}}{\mathfrak{C}} x_3^{(n)}\right)^2 + \left(\frac{\sqrt{\mathfrak{c}_1^2 + \mathfrak{c}_2^2}}{\mathfrak{D}} y_3^{(n)}\right)^2 = 1, \tag{C.7}$$

where $x_j^{(n)}$ and $y_j^{(n)}$ are the local coordinates used in Section C.1. Similar to the solutions presented in Section C.1, the trajectories of the nodal points along the $j = 1$ and $j = 3$ layers are also ellipses. These ellipses have axes aligned parallel and perpendicular to the j-th layer of the Dirichlet strip for $j = 1$ and $j = 3$, while the central nodal points ($j = 2$) exhibit only vertical motions.

At the crossing or touching points of the dispersion curves, the nodal points in the central layer ($j = 2$) move along elliptical trajectories or linear paths that are generally not aligned with the horizontal or vertical directions. In this case, the above representations of the displacement components for the central nodal points do not apply. Illustrative examples of the nodal point trajectories related to the dispersion degeneracies are provided in Appendix A. At the crossing or touching points of the dispersion curves, the phase velocity can be used to describe the direction of motion of the waveforms.

Appendix D. Non-chiral discrete Neumann lattice strip

In this appendix we examine the modes of a lattice strip, subjected to gravity, with Neumann boundary conditions in the absence of gyroscopic forces, corresponding to $\Omega = 0$ (see Section 3.3 of the main text). In this case, the dispersion equation can be written as product of two cubic polynomials in ω^2 as follows (see also (3.29)):

$$F_1(G,k,\omega)F_2(G,k,\omega) = 0, \tag{D.1}$$

where

$$\begin{aligned}
F_1(G,k,\omega) = \sigma_N^{(1)}|_{\Omega=0} &= m^3\omega^6 + (4c\cos(kl) - 3Gm - 7c)m^2\omega^4 \\
&+ \left(4c^2\cos^2(kl) - 4\left(2Gm + \frac{33}{8}c\right)c\cos(kl) + 3G^2m^2 + 14mcG + \frac{59c^2}{4}\right)m\omega^2 \\
&-4\left(Gm + \frac{9c}{8}\right)c^2\cos^2(kl) + 4\left(G^2m^2 + \frac{33}{8}Gcm + \frac{27}{8}c^2\right)c\cos(kl) - G^3m^3 - 7G^2cm^2 - \frac{59Gc^2m}{4} - 9c^3, \\
F_2(G,k,\omega) = \sigma_N^{(2)}|_{\Omega=0} &= m^3\omega^6 + (2m^2c\cos(kl) - 3Gm^3 - 7m^2c)\omega^4 \\
&+ \left(2\left(-2Gm^2 - \frac{21}{4}cm\right)c\cos(kl) + 3G^2m^3 + 14m^2cG + \frac{51c^2m}{4}\right)\omega^2 \\
&-\frac{9\cos^2(kl)c^3}{2} + 2\left(G^2m^2 + \frac{21}{4}Gcm + \frac{9}{2}c^2\right)c\cos(kl) - G^3m^3 - 7G^2cm^2 - \frac{51Gc^2m}{4} - \frac{9c^3}{2},
\end{aligned} \tag{D.2}$$

where $\sigma_N^{(1)}$ and $\sigma_N^{(2)}$ are defined by (3.30) and (3.31) in the main text.

The absence of spinners limits the coupling between the transverse displacement components of the nodal points; the nodal point trajectories are determined by their spring connections with their neighbouring nodal points and gravitational forces. For $\Omega = 0$, the lowest frequency mode occurs at $\omega = \sqrt{G}$ when $k = 0$, while the highest frequency of the vibrating non-chiral Neumann lattice strip occurs at $\omega = \sqrt{(4mG + 13c + \sqrt{73}c)/m/2}$ when $kl = \pm\pi$. In the following sections, we explore the dynamic features of the non-chiral Neumann lattice strip.

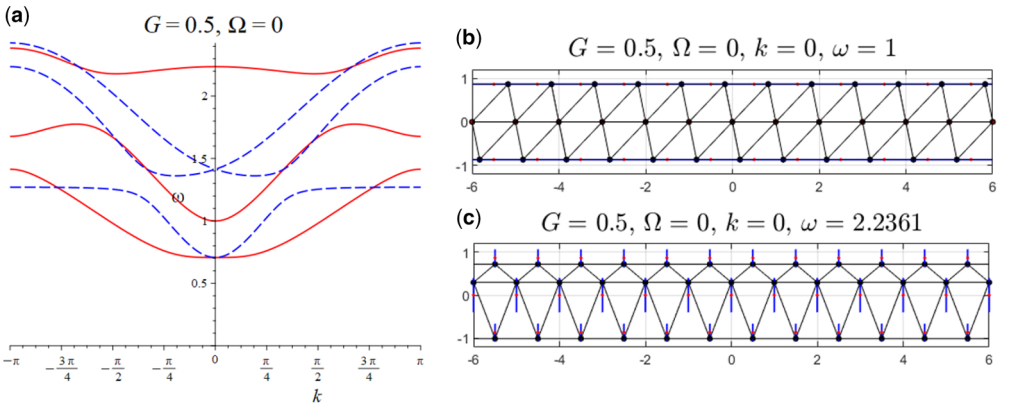

Fig. D1 (a) Dispersion diagram, showing ω versus k, for an infinite non-chiral Neumann lattice strip for $\Omega = 0$ and $G = 0.5$. The trajectories of the nodal points in the strip for $k = 0$ and two values of ω corresponding to the standing modes are illustrated in parts (b) and (c), where $\omega = 1$ and $\omega = 2.2361$, respectively

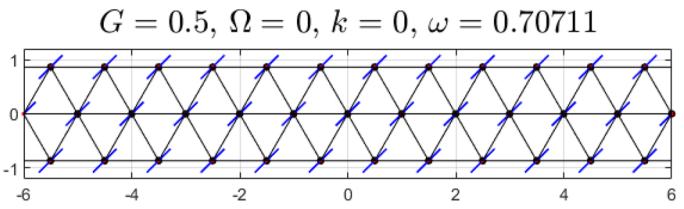

Fig. D2 Standing wave pattern in the non-chiral Neumann lattice strip for $k = 0$. The wavenumber and frequency of the oscillations at $(k, \omega) = (0, 0.70711)$ correspond to the touching point of the dispersion curves shown in Fig. D1(a)

D.1. Standing modes

In this section, we demonstrate the typical standing modes of the Neumann lattice strip subjected to gravity. We assume that gravity acts uniformly along the strip with $G = 0.5$, and that the gyricity is zero for each spinner ($\Omega = 0$). For simplicity, all remaining normalised parameter values of the structure are set to unity ($c = 1, l = 1$ and $m = 1$).

In Fig. D1(a), we present the dispersion diagram for a non-gyroscopic Neumann lattice strip with identical masses connected by massless unit-length springs. As discussed in the main text, a non-zero gravity parameter creates a low-frequency band gap in the range $0 \leq \omega < \sqrt{G}$ (≈ 0.7071). The cut-off frequency is $\omega = \sqrt{4G + 13 + \sqrt{73}}/2$ (≈ 2.4261), beyond which there are no propagating modes. In contrast, the propagating and standing waveforms occur for frequency values in the range $0.7071 \leq \omega \leq 2.4261$. Fig. D1b) and (c) show the standing modes of the non-chiral strip for two different frequency values at $k = 0$, leading to oscillation patterns with zero net energy transfer. In Fig. D1(b), the nodal points in the upper and lower layers of the strip oscillate horizontally, resembling the harmonic motion of a simple pendulum, while the central nodal points exhibit no vibrations. In the example shown in Fig. D1(c), the nodal points in the upper and lower layers move in opposite directions compared to the central nodal points, each displaying vertical movements. The trajectories

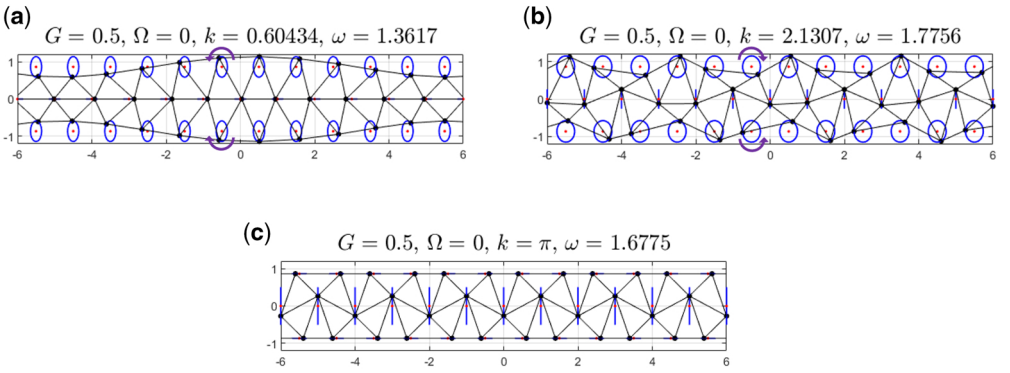

Fig. D3 Trajectories of the nodal points in the Neumann lattice strip in the absence of gyricity corresponding to standing waves with $k \neq 0$. The associated dispersion diagram is provided in Fig. D1(a): (a) $(k,\omega) = (0.60434, 1.3617)$, (b) $(k,\omega) = (2.1307, 1.7756)$ and (c) $(k,\omega) = (\pi, 1.6775)$. The circular arrows indicate the orientation of motion of the nodal points

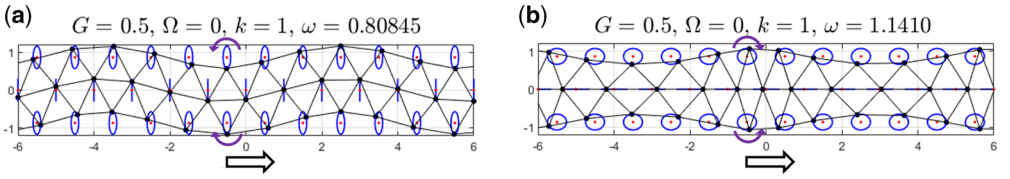

Fig. D4 Nodal trajectories of the non-chiral Neumann lattice strip for the parameter values $G = 0.5$ and $\Omega = 0$, corresponding to waves propagating in the positive x-direction along the strip: (a) $(k,\omega) = (1, 0.80845)$ and (b) $(k,\omega) = (1, 1.1410)$

of the nodal points can be viewed in the accompanying videos in the electronic Supplementary Material. The touching point between the solid and dashed dispersion curves for $k = 0$ occurs at $(k,\omega) = (0, 0.70711)$ (see also Section 3.3.2). This corresponds to a standing mode where the central nodal points are displaced in both horizontal and vertical directions as shown in Fig. D2.

The degeneracy point of the two high-frequency dashed curves shown in Fig. D1(a), along the frequency axis, corresponds to the vibration frequency $\omega = \sqrt{2}$ (≈ 1.4142). In this case, the structure can exhibit standing wave patterns. Standing waves for the non-chiral Neumann strip are also observed for non-zero wavenumbers as shown in Fig. D3. The trajectories of the nodal points in the upper ($j = 3$) and lower ($j = 1$) layers presented in Fig. D3(a) and (b) consist of ellipses with their major axes aligned perpendicular to the j-th layer. However, the eccentricities of the ellipses and the orientations of motion differ between the two examples. In addition, the central nodal points move horizontally in Fig. D3(a) and vertically in Fig. D3(b). An illustrative example of the standing mode at $k = \pi$ is displayed in Fig. D3(c), where the central nodal points move vertically, while the nodal points in the lower and upper layers move horizontally, differing from the elliptical paths shown in Fig. D3(a) and (b). In the presented examples of standing modes with $k > 0$, the central nodal points are displaced linearly and the phase velocities are positive. Although there are no gyroscopic effects, the spring connections and gravitational forces result in elliptical motions of the nodal points.

D.2. Propagating waveforms

We turn our attention to the propagating waves along the gravitational Neumann strip in the absence of gyricity. In this section, we provide two illustrative examples of the nodal point trajectories associated with propagating waves along the non-chiral strip. The parameter values used in the examples are identical to those in Section D.1, while the frequencies and wavenumbers correspond to the eigenmodes exhibiting propagating waves instead of standing waves. The corresponding dispersion diagram is shown in Fig. D1(a).

Figure D4 illustrates the nodal point trajectories of the non-chiral Neumann strip corresponding to propagating waves with a positive group velocity. The trajectories of the nodal points on the upper and lower layers are elliptical in both Fig. D4(a) and (b), while the central nodal points move vertically in Fig. D4(a) and horizontally in Fig. D4(b) (see also Section 3.3.2). It is also observed that since the group velocity is positive, the energy is transported along the direction of the wave propagation, that is in the positive x-direction. Due to the symmetry of the dispersion diagram shown in Fig. D1(a) relative to the frequency axis, a wave propagating in the negative x-direction can also be obtained by choosing the corresponding negative value of the wavenumber k compared to the examples presented in Fig. D4. The informative videos of the nodal point trajectories for the examples shown in Fig. D4 can be viewed in the electronic Supplementary Material.